

Very extended cold gas, star formation and outflows in the halo of a bright QSO at $z > 6$

C. Cicone^{1,2}, R. Maiolino^{1,2}, S. Gallerani³, R. Neri⁴, A. Ferrara³, E. Sturm⁵, F. Fiore⁶, E. Piconcelli⁶, and C. Feruglio⁴

¹ Cavendish Laboratory, University of Cambridge 19 J. J. Thomson Avenue, Cambridge CB3 0HE, UK
e-mail: c.cicone@mrao.cam.ac.uk

² Kavli Institute for Cosmology, University of Cambridge, Madingley Road, Cambridge CB3 0HA, UK

³ Scuola Normale Superiore, Piazza dei Cavalieri 7, 56126 Pisa, Italy

⁴ Institute de Radioastronomie Millimetrique (IRAM), 300 Rue de la Piscine, F-38406 St. Martin d'Heres, Grenoble, France

⁵ Max Planck Institute für Extraterrestrische Physik (MPE), Giessenbachstraße 1, 85748, Garching, Germany

⁶ Osservatorio Astronomico di Roma (INAF), via Frascati 33, I-00040 Monteporzio Catone, Italy

Received xx xx xx / Accepted: xx xx xx

ABSTRACT

Past observations of QSO host galaxies at $z > 6$ have found cold gas and star formation on compact scales of a few kiloparsecs. We present new high sensitivity IRAM PdBI follow-up observations of the [C II] 158 μm emission line and FIR continuum in the host galaxy of SDSS J1148+5152, a luminous QSO at redshift 6.4189. We find that a large fraction of the gas traced by [C II] is at high velocities, up to $\sim 1400 \text{ km s}^{-1}$ relative to the systemic velocity, confirming the presence of a major quasar-driven outflow indicated by previous observations. The outflow has a complex morphology and reaches a maximum projected radius of $\sim 30 \text{ kpc}$. The extreme spatial extent of the outflow allows us, for the first time in an external galaxy, to estimate mass-loss rate, kinetic power and momentum rate of the outflow as a function of the projected distance from the nucleus and the dynamical time-scale. These trends reveal multiple outflow events during the past 100 Myr, although the bulk of the mass, energy and momentum appear to have been released more recently, within the past $\sim 20 \text{ Myr}$. Surprisingly, we discover that also the quiescent gas at systemic velocity is extremely extended. More specifically, we find that, while 30% of the [C II] within $v \in (-200, 200) \text{ km s}^{-1}$ traces a compact component that is not resolved by our observations, 70% of the [C II] emission in this velocity range is extended, with a projected FWHM size of $17.4 \pm 1.4 \text{ kpc}$. We detect FIR continuum emission associated with both the compact and the extended [C II] components, although the extended FIR emission has a FWHM of $11 \pm 2 \text{ kpc}$, thus smaller than the extended [C II] source. Overall, our results indicate that the cold gas traced by [C II] is distributed up to $r \sim 30 \text{ kpc}$ in the host galaxy of SDSS J1148+5152. A large fraction of extended [C II] is likely associated with star formation occurring on large scales, but the [C II] source extends well beyond the FIR continuum, and additional multi-wavelengths observations are needed in order to clarify the origin of this most extended [C II].

Key words. galaxies: general – galaxies: ISM – galaxies: evolution – galaxies: high-redshift – quasars: general

1. Introduction

Recent millimetre observations have revealed that the host galaxies of high redshift luminous QSOs are quite compact, with extremely intense star formation confined within a few kiloparsecs in their nuclear regions, fed by large amounts of dense gas (e.g. see Carilli & Walter 2013 for a recent review). Moreover, high resolution interferometric observations of these high redshift sources have suggested the presence of regularly rotating and relatively undisturbed disks (Carniani et al. 2013; Wang et al. 2013), although in some cases they appear to be highly turbulent (De Breuck et al. 2014). Only in a few high- z QSOs, observations have revealed the presence of some diffuse gas at a distance of several kiloparsecs from the nucleus, possibly indicative of galaxy interactions (Gallerani et al. 2012). However, recent theoretical studies have concluded that, in order to reconcile the extreme properties (BH mass, dust and gas mass) of these high redshift quasars with early star formation occurring with a

standard IMF, the dynamical masses of these objects should be a factor of 3-30 higher than the maximum values allowed by observations (Valiante et al. 2011, 2014; Calura et al. 2014). This suggests that past millimetre observations may have missed a significant fraction of baryons in high redshift QSO host galaxies.

The collisionally-excited fine structure transition of $\text{C}^+ \text{ } ^2\text{P}_{3/2} \rightarrow \text{ } ^2\text{P}_{1/2}$ at rest-frame wavelength of $157.741 \mu\text{m}$ (hereafter [C II] 158 μm) is conveniently redshifted, at $z > 4$, into the sub-millimetre/millimetre atmospheric windows. The [C II] 158 μm is one of the brightest lines in the spectrum of star forming galaxies, as it is the dominant coolant of the ISM over a wide range of physical conditions. The ionisation potential of carbon is 11.26 eV, hence C^+ , HI and even H_2 usually coexist in the same medium, and indeed neutral hydrogen is the main collisional partner of C^+ . Although [C II] emission is commonly associated with star formation, the large variety of physical conditions in which C^+ can be produced and excited makes its interpreta-

tion not straightforward. This has been clearly shown by recent detailed studies of the spatial distribution of various gas tracers in the Milky Way and other few nearby galaxies, including Herschel observations of [C II]. In particular, in our Galaxy, only ~50% of the [C II] emission is associated with dense photon-dominated regions (PDRs) exposed to the FUV radiation field of young and massive stars (Pineda et al. 2013). A large fraction of [C II] (~30%) in the Milky Way is linked to “CO-dark” molecular hydrogen, which dominates the gas mass of diffuse molecular clouds, but it can also be an important component of some unshielded dense molecular clouds with large envelopes where the formation of CO is inhibited and most of the gas-phase carbon is found in C⁰ or C⁺ atoms (Wolfire et al. 2010; Langer et al. 2010, 2014; Velusamy et al. 2010; Pineda et al. 2013). Finally, Pineda et al. (2013) have shown that ~20% of [C II] is linked to diffuse atomic clouds (in particular to the cold neutral medium, CNM), and a low fraction (~4%) is associated with warm ionised medium (WIM). Further complicating its interpretation, [C II] can be enhanced by shocks (Appleton et al. 2013). Intriguingly, [C II] seems to be also a good tracer of outflows and, especially, of molecular gas in outflow (Fischer et al. 2010; Contursi et al. 2013; Kreckel et al. 2014).

The first high redshift source in which [C II] emission was ever detected (Maiolino et al. 2005), SDSS J1148+5152 at redshift 6.4189, is one of the most powerful quasars in the Universe, with an intrinsic bolometric luminosity of $L_{\text{AGN}} = 5.63 \times 10^{13} L_{\odot}$ (Schneider et al. 2014). This is the perfect laboratory to study the formation of the first massive galaxies and the coevolution of galaxies and black holes at the end of the reionization epoch. SDSS J1148+5152 was discovered through SDSS photometry (Fan et al. 2003), and since then it has been the subject of extensive multi-wavelength studies, aimed at constraining the extreme properties of its host galaxy and of its cosmological environment (e.g. Bertoldi et al. 2003; Walter et al. 2003, 2004; Willott et al. 2003; Riechers et al. 2009; Gallerani et al. 2010; Decarli et al. 2012; Carilli & Walter 2013). Walter et al. (2009) observed the [C II] emission line in SDSS J1148+5152 using the most extended configuration of the IRAM Plateau de Bure Interferometer (PdBI), and derived a size of 1.5 kpc, which, combined with the extreme FIR luminosity of this source, suggests the presence of a kpc-scale “hyper-starburst” in its nucleus, fed by large amounts of molecular gas. Moreover, SDSS J1148+5152 was also the first high redshift galaxy in which a powerful quasar-driven outflow was discovered (Maiolino et al. 2012). The outflow was revealed by the presence of extremely broad wings of the [C II] emission line, tracing gas at high velocities (v up to 1200 km s⁻¹), which appeared marginally resolved at a 2 arcsec resolution, with a measured (projected) diameter of ~ 16 kpc.

In this work we present new follow-up observations of the [C II] emission line and FIR continuum in SDSS J1148+5152, obtained with the C and D configuration of the IRAM PdBI (resulting in a synthesized beam size of 1.3''×1.2'' for the [C II] observations and of 1.1''×1.1'' for the FIR continuum observations), which enable us to investigate the properties of this source on large scales, with a sensitivity much higher than previous observations. Throughout the paper, we adopt a standard Λ CDM cosmological model with $H_0 = 67.3$ km s⁻¹Mpc⁻¹, $\Omega_{\Lambda} = 0.685$, $\Omega_{\text{M}} = 0.315$ (Planck Collaboration et al. 2013). With the adopted cosmology, at the redshift of SDSS J1148+5152, the physical scale is 5.623 kpc arcsec⁻¹, and the age of the Universe is 0.85 Gyr.

2. Observations

We have observed with the IRAM PdBI the [C II] 158 μ m line in the host galaxy of the luminous quasar SDSS J1148+5152. The pointing and phase centre of our observations corresponds to the SDSS optical position of the quasar (RA=11:48:16.64, Dec=52:51:50.30). At the redshift of the source ($z=6.4189$, Maiolino et al. (2005)), the [C II] 158 μ m transition is redshifted into the 1mm band, at an observed frequency of 256.175 GHz. The observations were obtained with the C configuration of the IRAM PdBI (with 6 antennas covering baselines from 16.6m to 176.0m) between November 2012 and April 2013 and were combined with the previous 2011 observations in D configuration (Maiolino et al. 2012), for a total on-source-time of 30 hrs. We reach a sensitivity of 0.46 mJy beam⁻¹ in channels of 100 km s⁻¹, which is unprecedented for observations of high redshift quasars at this frequency. The resulting synthesized beam-size using natural weighting is 1.3''×1.2'', and the PdBI primary beam, giving the field of view, at these frequencies is 19.7''×19.7''. Data reduction and analysis were performed by using the CLIC and MAPPING softwares within the GILDAS package. The flux calibration accuracy in the 1mm band is about 20% (Castro-Carrizo & Neri 2010). We used the wide-band (WideX) correlator offered by the PdBI, which provides a spectral resolution of 20 MHz (corresponding to 23.4 km s⁻¹) over its full bandwidth of 3.6 GHz. The 3.6 GHz spectral window was centred at 256.172 GHz (i.e. on the [C II] 158 μ m line) for all tracks but two, for which the centre was instead set at 256.672 GHz, hence providing an additional 0.5 GHz-wide window on the continuum blueward of the line.

In this work we also make use of ancillary C+D configuration IRAM PdBI observations of the FIR continuum of SDSS J1148+5152 at 262 GHz (rest frame wavelength $\lambda = 154.2$ μ m) and 259.4 GHz (rest frame wavelength $\lambda = 155.8$ μ m), carried out between May 2010 and December 2012. By merging the two datasets at 262 GHz and 259.4 GHz, we obtain a high sensitivity FIR continuum map (1 σ rms noise of 0.067 mJy beam⁻¹). The resulting synthesized beam-size using natural weighting is 1.1''×1.1''. These observations are part of a parallel project presented in a companion paper (Gallerani+14, in prep).

3. Results

3.1. The total [C II] 158 μ m emission

For the purpose of continuum subtraction, the rest-frame 157.7 μ m FIR continuum (observed frequency of 256 GHz) is estimated by collapsing the line-free channels of our wide-band IRAM PdBI observations, corresponding to the velocity ranges of $v \in (-2700, -2400)$ km s⁻¹, $v \in (-1900, -1500)$ km s⁻¹ and $v \in (1500, 2100)$ km s⁻¹. The uv plot of the continuum at 256 GHz is well fitted by a point (unresolved) source centered at RA=11:48:16.62 and Dec=52:51:50.22, with a flux density of 3.31 ± 0.18 mJy. We note that there is a small inconsistency between our new 157.7 μ m continuum estimate and the flux density of 4 mJy expected at these wavelengths from the bolometric observations of Bertoldi et al. (2003), as measured by Maiolino et al. (2012). This discrepancy was not evidenced in Maiolino et al. (2012) because of the larger error of their continuum measure, which was based on the D-configuration data only. It is possible that this small inconsistency with Bertoldi et al. (2003) is due to the presence of additional sources close to SDSS J1148+5152 included within the 10'6 MAMBO beam (FWHM).

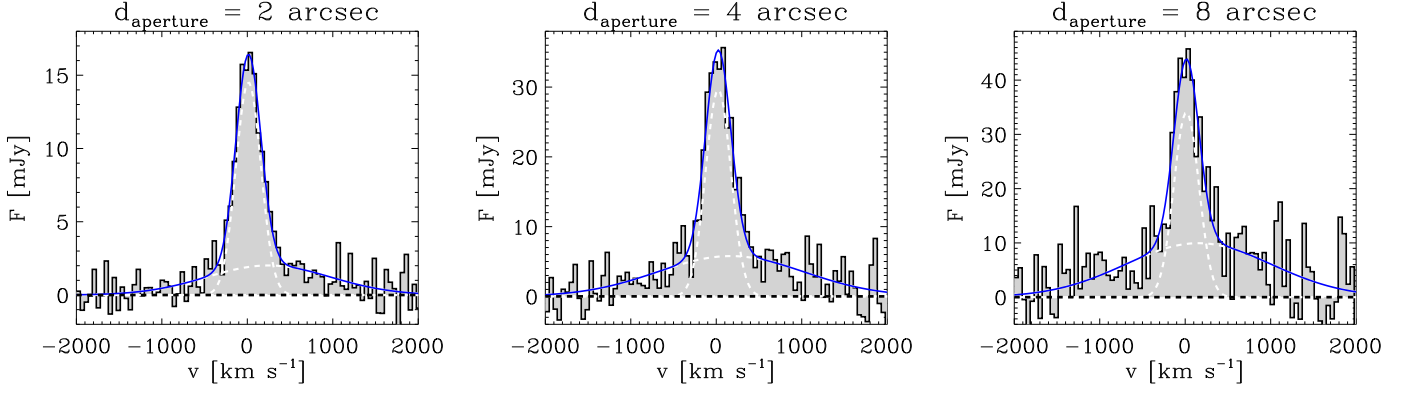


Fig. 1: IRAM PdBI continuum-subtracted spectrum of the [C II] 158 μ m emission line of SDSS J1148+5152. The three spectra shown have been extracted using different apertures, namely circular apertures with diameters of 2 arcsec (*left panel*), 4 arcsec (*central panel*) and 8 arcsec (*right panel*). Note the different scales on the y-axes in the three panels. For display purposes, the spectra have been re-binned by a factor of 2, corresponding to channels of 46.8 km s⁻¹. The Gaussian fits to the line profiles (using a narrow and a broad Gaussian component to fit respectively the narrow core, tracing quiescent gas, and the broad wings, tracing the outflow) are performed on the original non-binned spectra and the fits results are reported in Table 1.

Table 1: Results of the Gaussian fits to the [C II] 158 μ m emission line spectrum of SDSS J1148+5152:

Aperture [†]	Narrow component				Broad component				Total line
	v [km s ⁻¹]	σ_v [km s ⁻¹]	S_{peak} [mJy]	I_v [Jy km s ⁻¹]	v [km s ⁻¹]	σ_v [km s ⁻¹]	S_{peak} [mJy]	I_v [Jy km s ⁻¹]	I_v [Jy km s ⁻¹]
2 arcsec	13 ± 9	146 ± 11	14.5 ± 0.9	5.3 ± 0.5	250 ± 160	730 ± 170	2.0 ± 0.6	3.7 ± 1.4	9.0 ± 1.5
4 arcsec	24 ± 13	148 ± 16	30 ± 3	11.0 ± 1.5	170 ± 170	900 ± 200	5.8 ± 1.6	12 ± 5	23 ± 5
8 arcsec	14 ± 19	150 ± 20	34 ± 4	13 ± 3	200 ± 300	900 ± 300	10 ± 3	21 ± 9	34 ± 9

Notes: [†] Diameter of the circular aperture used to extract the spectrum, as in Fig. 1.

The channels between $v = -2400$ km s⁻¹ and $v = -1900$ km s⁻¹ are excluded from the continuum integration because of the presence of a putative feature, detected at the 4.2 σ level in the maps, whose position is shifted by 1.5 arcsec to the south with respect to the quasar optical position and whose origin is not clear from our data (it could be either part of the extended outflow discussed in Section 3.3 or associated with another galaxy).

Following the standard procedure, we subtract the continuum directly from the uv data, and we extract from the continuum-subtracted and cleaned data cube the spectrum of the [C II] 158 μ m emission line of SDSS J1148+5152. In Figure 1 we show the resulting continuum-subtracted spectra extracted using three circular apertures with diameters of 2 arcsec, 4 arcsec, and 8 arcsec. Note that the three plots in Fig. 1 have different scales on the y-axis.

Each spectrum in Fig. 1 is fit by using two Gaussians, e.g., a narrow Gaussian to fit the central core of the line, tracing quiescent gas, and a broad Gaussian to fit the broad wings, tracing the outflow discovered by Maiolino et al. (2012). The fit with two Gaussians is a simplistic model for the [C II] 158 μ m emission profile of SDSS J1148+5152, however it constitutes a good starting point for our study. The fit results are reported in Table 1. The widths of the two Gaussians used to fit the [C II] 158 μ m spectral profile show no significant variations between spectra

extracted from different apertures¹, and they are consistent with Maiolino et al. (2012).

Figure 1 and Table 1 clearly show that the contribution from an extended gas component to the total [C II] 158 μ m flux in SDSS J1148+5152 is significant. Indeed, the total integrated flux estimated by using the spectrum extracted from the 8 arcsec diameter aperture is significantly larger than the flux retrieved using the 4 arcsec aperture, and is almost *four* times as large as the flux measured from the 2 arcsec aperture. Such flux increment is observed in both the narrow and the broad Gaussians that are fit to the emission line profiles, suggesting that both components trace emission extended on *extremely* large scales ($d \gtrsim 4$ arcsec on sky, corresponding to $d \gtrsim 22$ kpc). However, we note that the largest flux variation with aperture size is observed in the broad wings of the [C II] 158 μ m line, confirming that the massive quasar-driven outflow is *very* extended.

The complex morphology and extreme spatial extent of the [C II] 158 μ m emission around this $z \sim 6.4$ QSO are clearly revealed by the map in Figure 2, obtained by collapsing the velocity channels spanning the full velocity extent of the emission line profile, i.e. from $v = -1400$ km s⁻¹ to $v = 1200$ km s⁻¹. The map shows a filamentary [C II] 158 μ m source, with structures extending in the radial direction up to the extraordinary (for a QSO host

¹ We note that all the six parameters of the fit are left as free parameters in the spectral fitting procedure. In particular, we did not constrain the fits performed on the spectra extracted from different apertures to have same widths, central velocities and/or amplitudes.

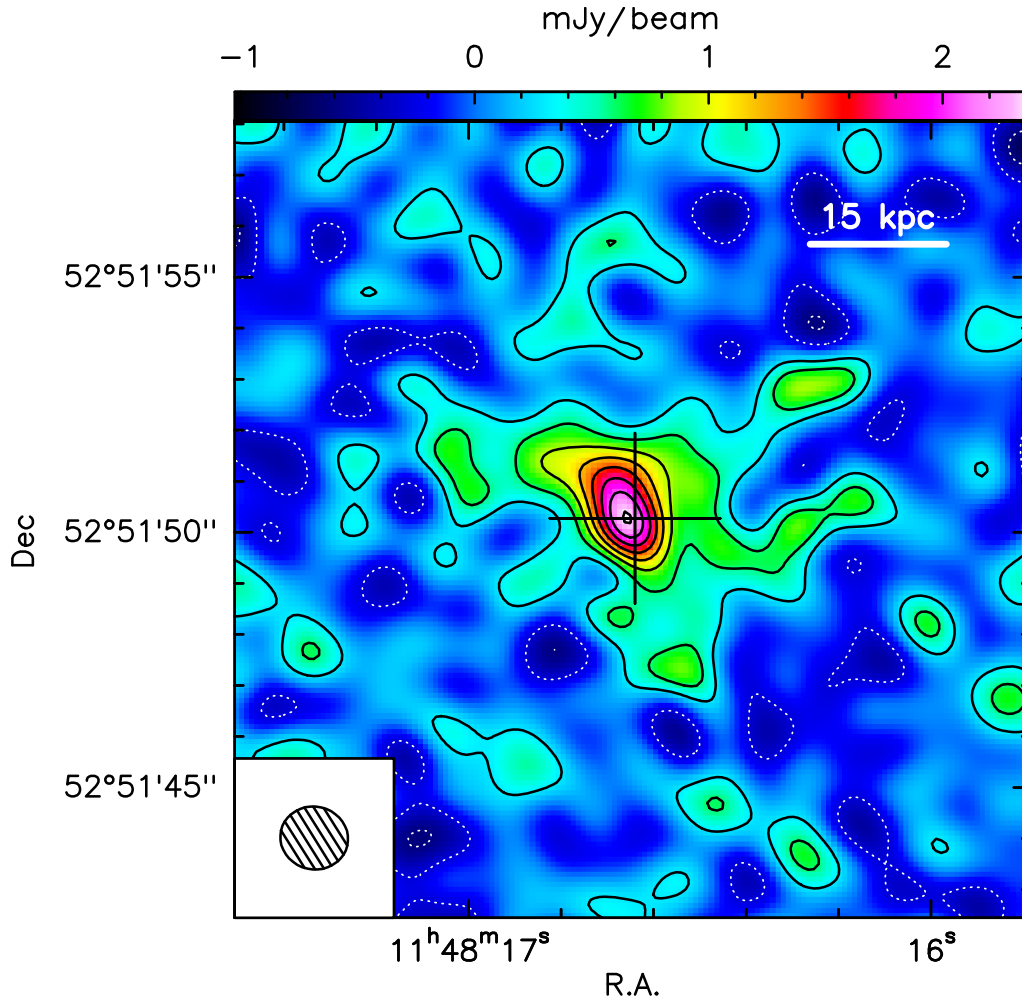


Fig. 2: IRAM PdBI continuum-subtracted map of the total [C II] 158μm emission of SDSS J1148+5152, integrated within $v \in (-1400, 1200)$ km s⁻¹. Negative and positive contours are in steps of 3σ (1σ rms noise is 0.26 Jy beam⁻¹ km s⁻¹). The synthesized beam ($1.3'' \times 1.2''$) is shown in the bottom left corner of the map. The cross indicates the pointing and phase centre, corresponding to the optical position of the quasar.

galaxy at $z = 6.4$) (projected) distances of $r \sim 30$ kpc from the QSO position (indicated by the cross).

The fits performed on the spectra extracted from different apertures (Figure 1 and Table 1) suggest that a large fraction of the [C II] 158μm emission at a distance $r > 2$ arcsec from the QSO (i.e. the emission that is not retrieved by using the 4 arcsec diameter aperture, but that is recovered with the largest 8 arcsec diameter aperture) is associated with the broad wings of the [C II] line, tracing a powerful quasar-driven outflow (Maiolino et al. 2012). We further investigate this in Fig. 3, where we show the same map as Fig. 2, in which we have marked the position of six regions (indicated with A-F) that are at a distance of $r \gtrsim 2$ arcsec from the emission peak. These regions represent the brightest features within the extended [C II] 158μm source. The spectra extracted from regions A-F (by using the elliptical apertures indicated in the map) are also shown in Fig. 3. The spectral fitting, performed by using multiple Gaussians (the fit results are reported in Table A.1 in Appendix A), shows that features A-F are characterised, on average, by high velocity dispersions and velocity offsets, suggesting an outflow origin.

However, there is also a large fraction of extended [C II] associated with “narrow” emission at systemic velocity (e.g. features B, C, F in Fig. 3), indicating the presence of extended

dynamically “quiescent” (i.e. non outflowing) [C II] -emitting gas outside of the central “hyper-starburst” detected by Walter et al. (2009). This extremely interesting - and unexpected - new prospect is investigated in Section 3.4. Interestingly, the narrow ($\sigma_v = 110 \pm 50$ km s⁻¹) feature in spectrum B with peak flux density of $S_{\text{peak}} = 2.7 \pm 1.0$ mJy is blue-shifted at a velocity of $v = -170 \pm 40$ km s⁻¹ (Table A.1). The shift in velocity, together with the low velocity dispersion and large distance from the nucleus, suggests that this feature may have a merger/inflow origin. This hypothesis is however difficult to test with the current data.

3.2. Comparison with previous observations

We note that the total [C II] 158μm velocity-integrated flux of 34 ± 9 Jy km s⁻¹ that we estimate from our IRAM PdBI observations (Table 1) is significantly larger than *any* previous flux measurement of [C II] obtained for this source. Such large discrepancy deserves further clarification, as these new observations significantly change the scenario presented by previous [C II] 158μm observations of SDSS J1148+5152 and of other high redshift quasars.

The first but only apparent flux inconsistency that we evidence is with the D-configuration data presented in Maiolino

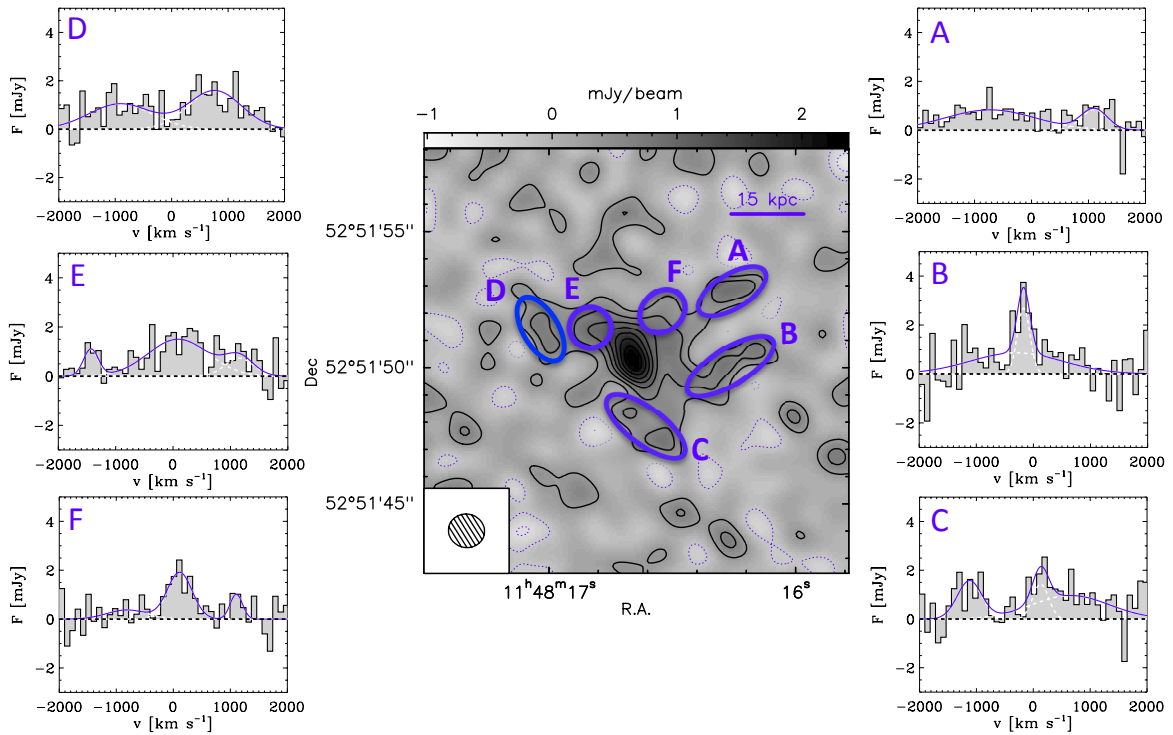


Fig. 3: IRAM PdBI continuum-subtracted map of the total [C II] $158\mu\text{m}$ emission of SDSS J1148+5152, integrated within $v \in (-1400, 1200) \text{ km s}^{-1}$, along with spectra extracted from different positions on the source. Negative and positive contours are in steps of 3σ (1σ rms noise is $0.26 \text{ Jy beam}^{-1} \text{ km s}^{-1}$). For display purposes, the spectra have been re-binned by a factor of 4, corresponding to channels of 93.6 km s^{-1} . The Gaussian fits to the line profiles are performed on the original non-binned spectra and the fits results are presented in Table A.1.

et al. (2012). The total flux derived by using the spectrum extracted from a 6 arcsec diameter aperture shown in Maiolino et al. (2012) is nearly a factor of two lower than our new estimate. We have reanalysed that dataset (which is also included in the final dataset used in this work), and we have concluded that the bulk of the flux loss was due to cleaning problems associated with the data cubes, with lower sensitivity, from which the spectra were extracted. Indeed, the discrepancy between the two datasets is much reduced (down to a $\lesssim 20\%$ flux discrepancy, likely associated with flux calibration issues in the 1mm band, Castro-Carrizo & Neri 2010) when estimating the fluxes from the UV data.

The discrepancy with Walter et al. (2009), who derived a flux of only $4.1 \pm 0.5 \text{ Jy km s}^{-1}$, can instead be almost entirely explained by the complex and extended nature of the source (Figure 2). These authors indeed observed SDSS J1148+5152 with the most extended configuration of the IRAM PdBI, therefore lacking short baselines and completely resolving out the extended [C II] $158\mu\text{m}$ emission. As a result, they only detected the [C II] $158\mu\text{m}$ flux associated with the central “hyper-starburst”, which is concentrated within a very compact region of $\sim 1.5 \text{ kpc}$ size. Moreover, due to their narrow bandwidth of $\Delta\nu = 1 \text{ GHz}$, the broad wings associated with the outflow could not be identified by Walter et al. (2009), and were subtracted from the line as continuum emission. This implies that also the flux of the narrow component was underestimated because the continuum level was overestimated, thereby causing an additional significant flux loss with respect to our new observations.

The origin of the discrepancy with the single-dish (IRAM 30m) flux measure by Maiolino et al. (2005) is more uncertain. Similarly to Walter et al. (2009), Maiolino et al. (2005) had a

bandwidth of only 1 GHz, and so they also subtracted the broad wings from the baselines as continuum emission. However, even taking into account the flux loss due to the wings subtraction, there is still an inconsistency of more than a factor of 2 with respect to our estimate. As a consequence, we suspect that the early [C II] $158\mu\text{m}$ detection in SDSS J1148+5152 by Maiolino et al. (2005) was affected by some calibration issues. In particular, pointing uncertainties may have played an important role. Indeed, the IRAM 30m absolute pointing uncertainties (in 2004) are comparable with the IRAM 30m beam at 256 GHz. The lack of bright sources close to SDSS J1148+5152, suitable for pointing calibration, had forced the use of pointing calibration sources far away from the target, which may have affected significantly the final pointing accuracy.

3.3. The resolved [CII] outflow

The [C II] $158\mu\text{m}$ spectrum of SDSS J1148+5152 exhibits extremely broad ($\text{FWHM} = 2100 \pm 500 \text{ km s}^{-1}$) wings, superimposed on a narrower core with $\text{FWHM} = 350 \pm 50 \text{ km s}^{-1}$ (Figure 1). The broad wings of the [C II] $158\mu\text{m}$ line, discovered by Maiolino et al. (2012), are believed to trace the most distant and powerful quasar-driven outflow ever detected. The outflow is also extremely extended. This could already be inferred from the low spatial resolution (synthesised beam of $2.2'' \times 1.8''$) observations presented in Maiolino et al. (2012), which marginally resolved the emission associated with the broad wings, providing a rough estimate for the outflow size (FWHM) of 2.9 arcsec.

Our new, higher resolution IRAM PdBI observations fully resolve the [C II] $158\mu\text{m}$ outflow of SDSS J1148+5152. In the

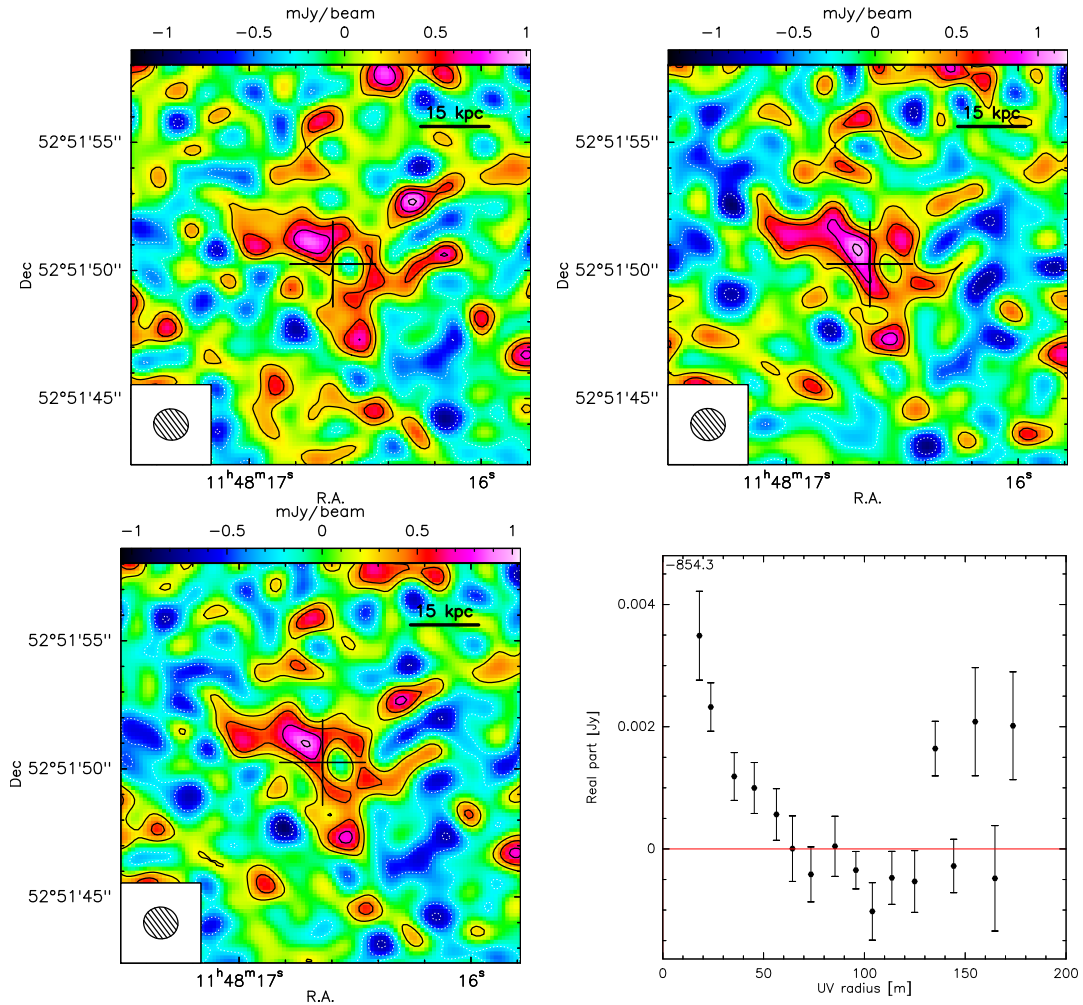


Fig. 4: *Top panels*: IRAM PdBI continuum-subtracted maps of the blue (*left*) and red (*right*) wings of the [C II] 158μm line of SDSS J1148+5152, integrated within $v \in (-1400, -300)$ km s $^{-1}$ and $v \in (400, 1200)$ km s $^{-1}$, respectively. Negative and positive contours are in steps of 1.5σ (1σ rms is 0.17 Jy beam $^{-1}$ km s $^{-1}$ and 0.14 Jy beam $^{-1}$ km s $^{-1}$ for the blue and red wing, respectively). *Bottom panels*: Map of the blue and red wings merged together (*left*) and corresponding uv plot (*right*). In the map of the merged wings, negative and positive contours are in steps of 2σ (1σ rms is 0.21 Jy beam $^{-1}$ km s $^{-1}$). The uv plot shows the real part of visibilities as a function of the uv distance, binned in baseline steps of 10m.

top panels of Figure 4 we show the continuum-subtracted maps of the blue and red wings of the [C II] line, integrated within $v \in (-1400, -300)$ km s $^{-1}$ and $v \in (400, 1200)$ km s $^{-1}$, respectively. We also report in the bottom-left panel of Fig. 4 the map of the wings merged together, similarly to Maiolino et al. (2012). As already suggested by the analysis of the spectra extracted from different apertures (Figure 1 and Table 1), the maps unambiguously show that the wings are extremely extended, and in particular that they are even more extended than what initially estimated by Maiolino et al. (2012). The bottom-right panel of Fig. 4 shows the real part of the visibilities of the broad wings as a function of the uv baseline radius (also known as “ uv plot”). The steeply declining trend clearly confirms that the broad wings are extended and resolved by our observations at high significance, and that they are not an artefact of the cleaning process. The fluctuations observed at large uv radii indicate that the morphology of the source is complex, consistently with the complexity of the structures revealed by the maps.

The maps of the blue and red wings of the [C II] 158μm emission (upper panels of Fig. 4) indicate that the blueshifted and the redshifted sides of the outflow are generally co-spatial. Indeed,

the two maps trace the same butterfly-shaped structure, although some blobs appear brighter in the blue component than in the red one and viceversa. We note that the spatial correspondence between blueshifted and redshifted wings rules out the hypothesis that companion galaxies with different systemic velocities are at the origin of the bulk of the broad [C II] 158μm emission, leaving a massive and extended outflow as the only viable explanation.

3.3.1. Outflow velocity and dynamical time-scale

In Maiolino et al. (2012) the outflow was only marginally resolved, and the outflow mass-loss rate of $\dot{M}_{\text{out}} \gtrsim 3500 M_{\odot} \text{ yr}^{-1}$ was estimated by assuming a spherical and/or multi-conical geometry. In the model adopted by Maiolino et al. (2012), the outflow rate was given by $\dot{M}_{\text{out}} = 3vM_{\text{out}}/R$, where v is the outflow velocity, M_{out} is the mass of atomic gas in outflow (estimated from the [C II] 158μm flux in the broad wings), and R is the radius of the broad wings emission (obtained by fitting the uv plot of the broad wings with a circular Gaussian model). However, our new, higher resolution IRAM PdBI observations allow us to fully resolve the outflow, hence enabling a much more de-

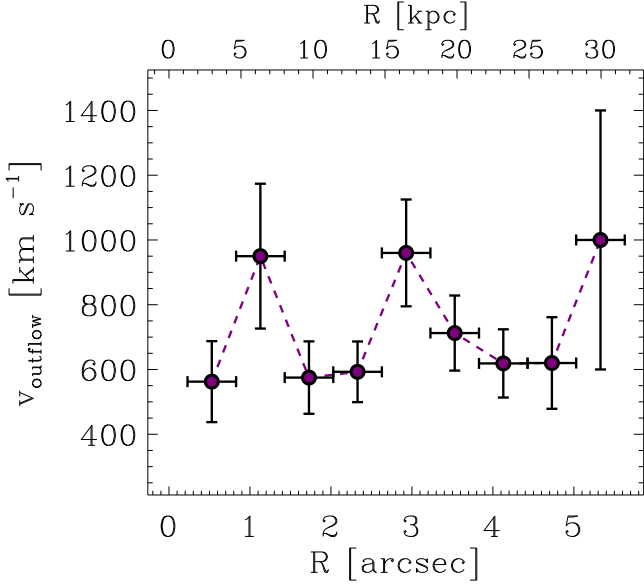


Fig. 5: Outflow velocity as a function of the radial distance from the QSO position. Both R and v are projected quantities. To produce this plot, the outflowing clumps have been divided into bins of radial distance from the QSO ($\Delta R = 0.6$ arcsec, i.e. ≈ 3 kpc). The plot shows the average velocity of the clumps within each bin ($\langle v \rangle = \sum_{i=1}^N v_i$, where N is the number of clumps in each bin). The error bars in the x direction indicate the bin size. The error on $\langle v \rangle$ is given by $\sigma_{\langle v \rangle} = (\sum_{i=1}^N \sigma_{v_i}^2)^{1/2} / N$, where σ_{v_i} is the uncertainty on the average velocity v_i of a clump in outflow, estimated as explained in Appendix B.

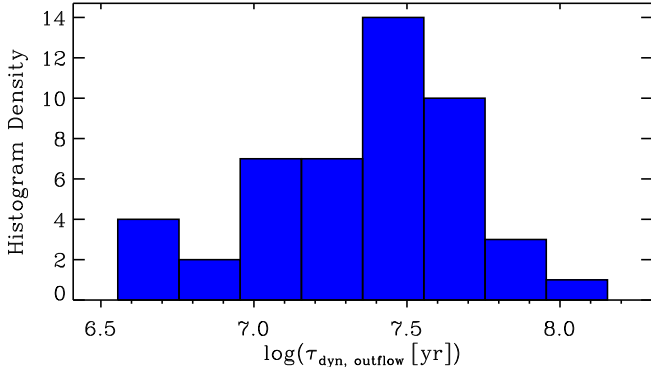


Fig. 6: Distribution of dynamical time-scales ($\tau_{\text{dyn}} = R/v$, where R is the projected distance from the central QSO and v is the outflow velocity) within the outflow, obtained for the individual outflowing clumps as described in Section 3.3 and in Appendix B.

tailed characterisation of the outflow properties, which was not possible with the previous dataset. The complex morphology revealed by the new maps of the outflow (Figure 4) is clearly *not consistent* with the simple spherical or multi-conical geometry assumed by Maiolino et al. (2012). Any attempt of modelling the [C II] outflow in SDSS J1148+5152 based on the current data would require a different, more complex geometry, and the uncertainties on such model would be very large. For this reason, in this paper, we decide to abstain from a simplistic modelling of the outflow geometry and instead we adopt a different, “resolved” approach to estimate the outflow properties.

Our approach is described in detail in Appendix B, and is based on measuring the dynamical time-scales of individual “blobs” of [C II] emission within the outflow². More specifically, we produce channel maps centred at different velocities, spanning the entire velocity range corresponding to the red and blue wings of the [C II] 158 μm line, tracing the outflow in the host galaxy of SDSS J1148+5152. The outflow channel maps are shown in Figure B.1. In these maps, we identify 48 “clumps” belonging to the outflow, as explained in Appendix B. For each clump in outflow we estimate its average (projected) velocity (v), its (projected) distance from the QSO (R), and its [C II] flux, which is used to estimate the mass of (atomic) gas in outflow as explained in the next section (Section 3.3.2). The dynamical time-scale of a clump in outflow is therefore simply given by $\tau_{\text{dyn}} = R/v$. We note that, by applying this definition, we are implicitly assuming that the velocity v of the clumps is constant throughout the outflow.

The relationship between the velocity and the distance from the QSO of the clumps in outflow is shown in Figure 5. The average velocity of the outflowing blobs does not depend on R , suggesting that the outflow is not significantly accelerating and/or decelerating. This also supports the definition of dynamical time-scales given above. The distribution of τ_{dyn} within the outflow is reported in Fig. 6; the histogram shows a slightly skewed left distribution, with median of $\tau_{\text{dyn}}^{\text{median}} = 10^{7.4}$ yr, but spanning a broad range from $\tau_{\text{dyn}}^{\text{min}} = 10^{6.6}$ yr to $\tau_{\text{dyn}}^{\text{max}} = 10^{8.0}$ yr. This indicates that the outflow has been in place for ~ 100 Myr, which is a non-negligible fraction of the age of the Universe at this redshift (i.e. 850 Myr with the adopted cosmology).

One should note that our measurement of τ_{dyn} neglects projection effects, more specifically, the fact that the *observed* distance R of the clumps from the centre is the projected distance, and that the *observed* velocity is actually only the component along our line of sight. As a consequence, the dynamical time-scales should be corrected by a factor $|\tan \phi|^{-1}$, i.e. $\tau_{\text{dyn}}(\text{real}) = \tau_{\text{dyn}}(\text{obs}) / |\tan \phi|$, where ϕ is the angle between our line of sight and the outflow direction of each individual cloud. Obviously ϕ is not known. However, if we assume that the outflow is isotropic, then the correction factor averaged over the entire solid angle, $\langle \frac{1}{|\tan \phi|} \rangle = \frac{1}{4\pi} \int_{4\pi} |\tan \phi|^{-1} d\Omega$, is equal to unity. Therefore, although the dynamical time-scales may need to be corrected by a significant factor for the individual clumps, the global average trends should not be affected significantly.

3.3.2. Integrated outflow mass-loss rate, kinetic power and momentum rate

In order to calculate the outflow mass-loss rate, we need to estimate the mass of gas carried by the outflow. To do this, we first measure the [C II] flux associated with each outflowing clump, as explained in Appendix B. The relationship between [C II] luminosity and gas mass depends on the gas density, temperature and abundance of C^+ ions (X_{C^+}). Lacking additional information on the physical conditions of the gas in outflow, we use the formula provided by Hailey-Dunsheath et al. (2010) to convert the [C II] luminosity into atomic gas mass, obtained under the hypothesis of optically thin [C II] emission. As in Maiolino et al. (2012), we assume that $X_{\text{C}^+} = 1.4 \times 10^{-4}$, $T = 200$ K, and $n \gg n_{\text{crit}}$

² We note that in this work we use also the term “clumps” to refer to the blobs of [C II] emission detected in outflow. The reader should be aware that these clumps or blobs generally do not correspond to individual clouds, as the minimum physical size probed by our observations (given by the synthesized beam) is ~ 6 -7 kpc.

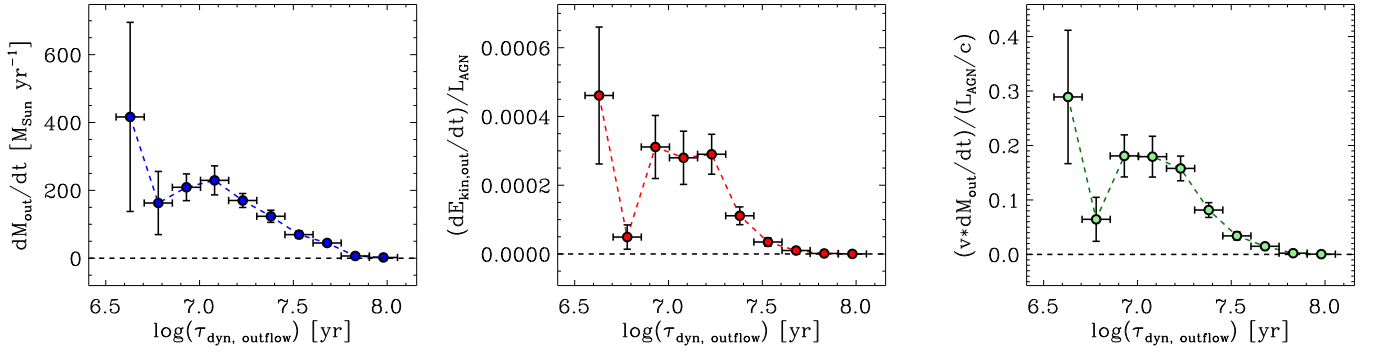


Fig. 7: Outflow mass-loss rate \dot{M}_{out} (left), kinetic power ratio $(1/2\dot{M}_{\text{out}}v^2)/L_{\text{AGN}}$ (centre) and momentum rate ratio $(\dot{M}_{\text{out}}v)/(L_{\text{AGN}}/c)$ (right) as a function of the dynamical time-scale of the clumps in outflow. These plots have been obtained by dividing the outflowing clumps (see Section 3.3) in bins of $\Delta\log(\tau_{\text{dyn}}) = 0.15$. The plots show, in correspondence of the average τ_{dyn} of each bin, the total \dot{M}_{out} , $(1/2\dot{M}_{\text{out}}v^2)/L_{\text{AGN}}$ and $(\dot{M}_{\text{out}}v)/(L_{\text{AGN}}/c)$ obtained by adding up the contribution of all the outflowing clumps within the bin. The error bars in the x direction indicate the bin size, i.e. $\Delta x = \pm 0.075$. The error bars in the y direction are calculated using the statistical error propagation (i.e. by propagating the errors on v , R and on the $[\text{C II}]$ fluxes measured for each clump in outflow, which are estimated in Appendix B). The errors do not take into account the uncertainty on the conversion from the $[\text{C II}]$ luminosity to atomic gas mass and the uncertainty on the AGN luminosity estimate (Schneider et al. 2014).

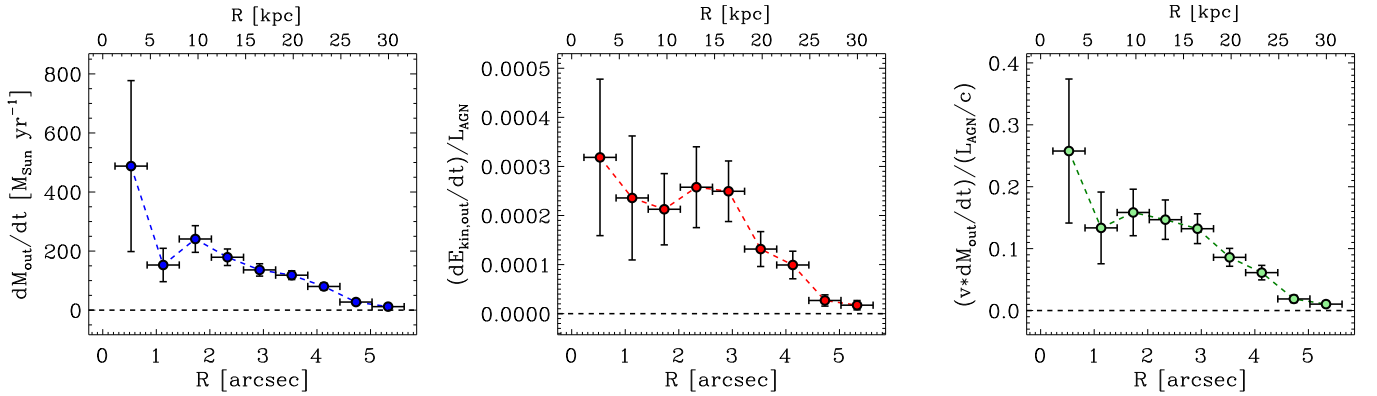


Fig. 8: Outflow mass-loss rate \dot{M}_{out} (left), kinetic power ratio $(1/2\dot{M}_{\text{out}}v^2)/L_{\text{AGN}}$ (centre) and momentum rate ratio $(\dot{M}_{\text{out}}v)/(L_{\text{AGN}}/c)$ (right) as a function of the projected distance from the QSO position. These plots have been obtained by dividing the outflowing clumps (see Section 3.3) in bins of $\Delta R = 0.6$ arcsec, corresponding to ≈ 3 kpc. The plots show, in correspondence of the average R of each bin, the total \dot{M}_{out} , $(1/2\dot{M}_{\text{out}}v^2)/L_{\text{AGN}}$ and $(\dot{M}_{\text{out}}v)/(L_{\text{AGN}}/c)$ obtained by adding up the contribution of all the outflowing clumps within the bin. For an explanation of the error bars, see caption of Figure 7.

($n_{\text{crit}} \sim 3 \times 10^3 \text{ cm}^{-3}$), typical of photo-dissociated regions (PDRs), and that 70% of the $[\text{C II}]$ flux arises from such medium (while the remaining 30% arises from other ISM phases).

The integrated outflow rate that we obtain by adding up the mass-loss rate contribution (i.e. $\dot{M}_{\text{out}} = M_{\text{out}}/\tau_{\text{dyn}}$) from all of the outflowing clumps is $1400 \pm 300 M_{\odot} \text{ yr}^{-1}$. The error on \dot{M}_{out} (see Appendix B for the details), does not take into account the uncertainty on the conversion from $[\text{C II}]$ luminosity to atomic gas mass. We stress that our measurement should be considered as a *lower limit* on the total outflow mass-loss rate, in first place because of the conservative assumptions we made for estimating the atomic gas mass from the $[\text{C II}]$ luminosity, and in second place because it only accounts for the atomic gas phase of the outflow, while a significant fraction of the mass in outflow may be in the molecular phase, similarly to local ULIRGs (e.g. Ciccone et al. (2014) and refs therein).

The integrated outflow mass-loss rate measured using this “resolved” approach is over a factor of 2 lower than the previous estimate by Maiolino et al. (2012), which was based on lower resolution and lower sensitivity data and relied on a sim-

plistic model for the outflow geometry. Conversely, our new method for estimating the outflow mass-loss rate, described in Section 3.3.1 and in Appendix B, does not assume any model for the outflow geometry. Furthermore, the outflow size estimated by Maiolino et al. (2012) by fitting the uv data with a simple Gaussian model is of only $R \approx 1.5$ arcsec (≈ 8 kpc), i.e. half the average $\langle R \rangle \approx 3$ arcsec that we measure by applying our “resolved” approach to the new dataset. It is therefore not surprising that our revised estimate of the outflow mass-loss rate in SDSS J1148+5152 is lower than the value that was obtained by Maiolino et al. (2012), although our estimate should be considered a lower limit as explained above.

We estimate the integrated kinetic power and momentum rate of the outflow by summing up the contribution from all outflowing clumps. Specifically, the sum of $1/2\dot{M}_{\text{out}}v^2$ and $\dot{M}_{\text{out}}v$, evaluated separately for each blob in outflow, gives, respectively, an integrated outflow kinetic power of $(3.3 \pm 0.5) \times 10^{44} \text{ erg s}^{-1}$ and an integrated outflow momentum rate of $(7.2 \pm 1.0) \times 10^{36} \text{ g cm s}^{-2}$. It is common practice in studies of AGN-driven outflows to compare these quantities with the AGN bolometric luminosity (L_{AGN}) and with the total radiative momentum output

from the AGN (L_{AGN}/c). In this case, by using the intrinsic AGN luminosity of $L_{\text{AGN}} = 5.63 \times 10^{13} L_{\odot}$ inferred by Schneider et al. (2014) for SDSS J1148+5152, the ratio between our estimate of the outflow kinetic power and L_{AGN} is $(1.6 \pm 0.2) \times 10^{-3}$, and the ratio between the momentum rate and L_{AGN}/c is 1.00 ± 0.14 . These values and their implications will be discussed in Section 4.1.

3.3.3. Outflow properties as a function of τ_{dyn} and R

In Section 3.3.2 we have derived the integrated outflow mass-loss rate, kinetic power and momentum rate. However, one may argue that given the quite broad distribution in dynamical time-scales within the outflow evidenced in Fig. 6, the clumps were not ejected all at the same time as a consequence of a single, explosive event, but, instead, they may have been expelled from the galaxy at different epochs. It is therefore interesting to investigate the contribution to the mass-loss rate, kinetic power and momentum rate of the outflow from clumps with different “ages”, i.e. with different τ_{dyn} . To this end, we present in Figure 7 the mass-loss rate, the kinetic power ratio $(1/2\dot{M}_{\text{out}}v^2)/L_{\text{AGN}}$ and momentum rate ratio $(\dot{M}_{\text{out}}v)/(L_{\text{AGN}}/c)$ of the outflow as a function of the dynamical time-scale of the outflowing clumps. Figure 7 suggests that the ejection of gas has not occurred at a constant rate in SDSS J1148+5152. In particular, the most extreme outflow event seems to have happened more recently, within the past ~ 5 Myr, as indicated by the first prominent peak of outflow mass-loss rate, kinetic power and momentum flux in Fig. 7. Interestingly, Fig. 7 shows the presence of a second, broader peak of these outflow properties between $\tau_{\text{dyn}} \in (8 - 20)$ Myr. Taken at face value, these findings would imply that, although the outflow may have been in place for 100 Myr, the bulk of the mass, energy and momentum have been released throughout two major outflow events happened more recently, within the past ~ 20 Myr (Figure 7).

A similar non-uniform distribution of the outflow mass-loss rate, kinetic power and momentum rate is evidenced also as a function of the (projected) distance from the QSO, as shown by Fig. 8, in which we report the radial profiles of the outflow properties. Figure 8 indicates that, overall, \dot{M}_{out} , $(1/2\dot{M}_{\text{out}}v^2)/L_{\text{AGN}}$ and $(\dot{M}_{\text{out}}v)/(L_{\text{AGN}}/c)$ decrease with the distance from the QSO. The main peak can be identified at projected radial distance of ~ 0.5 arcsec from the position of the central QSO, corresponding to ~ 3 kpc. There is also marginal evidence for a second, broad peak between $r \in (1.5 - 3)$ arcsec (i.e. $r \in (8 - 17)$ kpc). Similarly to what suggested for Fig. 7, the two peaks in Fig. 8 may be associated to major outflow events during the recent life of the QSO-galaxy. However, the significance of the second peak at $r \in (8 - 17)$ kpc is low, so this interpretation should be taken with caution. Figure 8 can be readily compared with the predictions of recent theoretical studies of AGN feedback (Costa et al. 2014; Thompson et al. 2014). This discussion is presented in Section 4.1.

We stress that observations are naturally limited for large R (and hence for high τ_{dyn}): indeed, outflow clumps at large distances from the galaxy centre are more difficult to probe due to the sensitivity of our maps. The lowest outflow velocities (which can also give high values of τ_{dyn}) are also difficult to probe due to contamination by quiescent gas, i.e. the narrow component of the [C II] line. In addition, “old” outflowing clumps, associated with longer dynamical time-scales and typically at larger distances, are more likely to have dissolved or evaporated. Therefore, the decreasing outflow rate with τ_{dyn} and radius may be

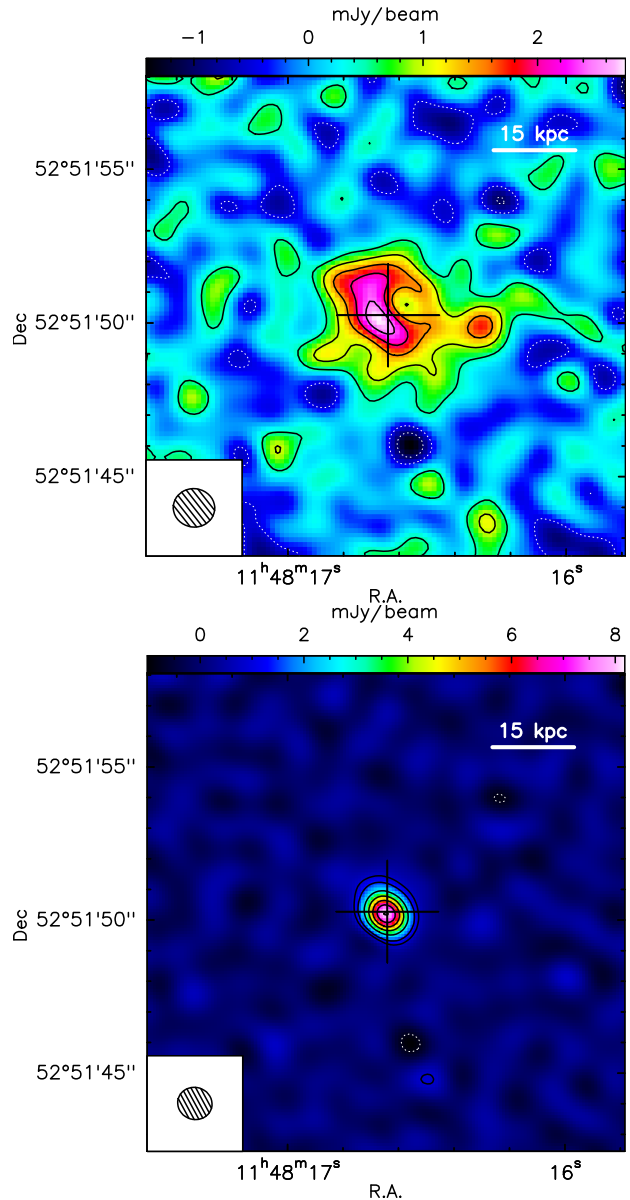


Fig. 10: Maps of the extended (*top*) and compact (*bottom*) components that contribute to the core [C II] $158\mu\text{m}$ emission of SDSS J1148+5152 within $v \in (-200, 200) \text{ km s}^{-1}$. The map of the extended component has been obtained by subtracting from the uv data the point source model fit. The map of the compact component has been produced by applying a uv tapering that cuts the visibilities with uv radius < 80 m; this operation increases the spatial resolution of the data (the resulting beam size is $1.1'' \times 1.1''$). Negative and positive contours are in steps of 2σ for the extended component in the top panel (1σ rms noise of $0.10 \text{ Jy beam}^{-1} \text{ km s}^{-1}$). For the compact component in the bottom panel, contours correspond to -3σ , 3σ , 5σ to 30σ in steps of 5σ (1σ rms noise of $0.11 \text{ Jy beam}^{-1} \text{ km s}^{-1}$).

in part the result of sensitivity issues in the observations and/or of the effect of outflowing clouds dissolving as they travel to larger distances, or being decelerated by the interaction with the intergalactic and circumgalactic media. For similar reasons, it is difficult to assess with the current data whether the outflow in SDSS J1148+5152 manages to escape the viral radius of the host galaxy and to enrich the IGM.

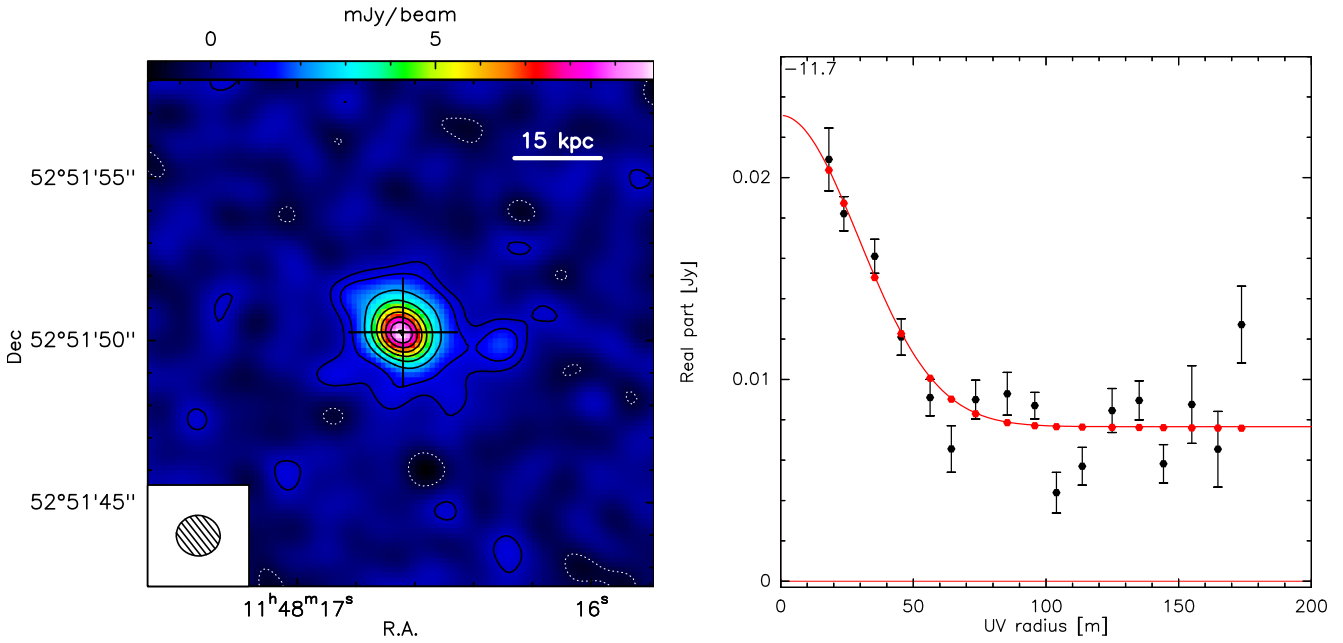


Fig. 9: IRAM PdBI continuum-subtracted map (*left*) and *uv* plane analysis (*right*) of the core of the [C II] 158 μ m emission line of SDSS J1148+5152, integrated within $v \in (-200, 200)$ km s $^{-1}$. *Left*: Negative and positive contours correspond to -3σ , 3σ , 5σ to 40σ in steps of 5σ (1σ rms noise is 0.10 Jy beam $^{-1}$ km s $^{-1}$). *Right*: Real part of visibilities as a function of the *uv* distance (*uv* plot), binned in baseline steps of 10m. The red curve indicates the best fit to the *uv* plot, which corresponds to the sum of two components: a point (unresolved) source, responsible for the flattening of the visibilities at large *uv* radii (*uv* radii > 50 m), and an extended (resolved) source fitted with a circular Gaussian model, which is responsible for the sharp decline of the visibilities at small *uv* radii.

3.4. Quiescent (narrow) [C II] emission

The map of the narrow component of the [C II] 158 μ m emission, integrated within $v \in (-200, 200)$ km s $^{-1}$, is presented in Figure 9. The source is resolved at high significance by our PdBI observations, and it appears surprisingly extended, on scales ≥ 20 kpc. This could already be inferred from the spectra extracted from different apertures, which showed that the flux of the narrow component is a factor of ~ 2 larger in the 4 arcsec aperture spectrum with respect to the 2 arcsec aperture spectrum (Figure 1 and Table 1).

The *uv* plot of the narrow [C II] 158 μ m emission, in the right panel of Fig. 9, provides important information about the structure of the source. In particular, the *uv* plot clearly shows the presence of two components: a compact component (not resolved), which is responsible for the flattening of the *uv* visibility amplitude at large (> 50 m) *uv* radii, and an extended component (resolved at high significance), which is at the origin of the decreasing trend of the *uv* visibility amplitude with radius at small *uv* radii. The red curve represents our best fit model, which is obtained by fitting the compact component with a point source and the resolved component with a circular Gaussian distribution. The resulting FWHM size of the circular Gaussian model is (3.1 ± 0.3) arcsec, corresponding to (17.4 ± 1.7) kpc. The velocity-integrated fluxes derived from the *uv* modelling are (6.2 ± 0.6) Jy km s $^{-1}$ and (3.08 ± 0.12) Jy km s $^{-1}$ for the resolved/extended and point sources, respectively. These fluxes can be translated into [C II] luminosities of $L_{[\text{CII}],\text{ext}} = (6.7 \pm 0.7) \times 10^9 L_{\odot}$ and $L_{[\text{CII}],\text{point}} = (3.33 \pm 0.13) \times 10^9 L_{\odot}$. Strikingly, the *uv* fit indicates that about 70% of the total [C II] emission at velocities $v \in (-200, 200)$ km s $^{-1}$ is in the extended component. We note that, however, the quality of the data does not allow us to dis-

tinguish between different models for the extended source. In particular, an exponential intensity distribution would also provide a good fit to the resolved component.

The extended and compact components contributing to the narrow [C II] emission within $v \in (-200, 200)$ km s $^{-1}$ can be disentangled in the *uv* plane and, therefore, imaged separately, by using the model fit shown in Fig. 9. In the upper panel of Fig. 10 we show the map of the extended component, obtained by subtracting from the *uv* data the point source model fit. The map shows an irregular ring-like and filamentary structure, with the most prominent filament extending up to $r \sim 28$ kpc (5 arcsec) in the western direction with respect to the QSO position. The centroid of the extended source is slightly shifted to the south-east with respect to the optical QSO position (indicated by the cross). The map of the compact component is shown in the bottom panel of Fig. 10, and it has been obtained by applying a *uv* tapering that cuts the visibilities with *uv* radius < 80 m. This bright, compact source, unresolved in our data and peaking at the QSO position, had already been detected and imaged by Walter et al. (2009) and it is likely tracing a kpc-scale hyper-starburst in the centre of SDSS J1148+5152.

We find no evidence for a regular rotation pattern in our IRAM PdBI [C II] maps (Appendix C). A spatial shift between the blue- and the red-shifted sides of the [C II] line was found in previous high resolution interferometric [C II] observations by Walter et al. (2009), which we now know that were resolving out a large fraction of extended [C II] flux ($\sim 70\%$ within $v \in (-200, 200)$ km s $^{-1}$ as shown by our *uv* fit in Fig. 9). While the compact source, which is not resolved by our observations, is probably rotationally-broadened as suggested by Walter et al. (2009), the hypothesis of rotation does not seem to hold for the dominant extended component, as shown in Fig. C.1, although

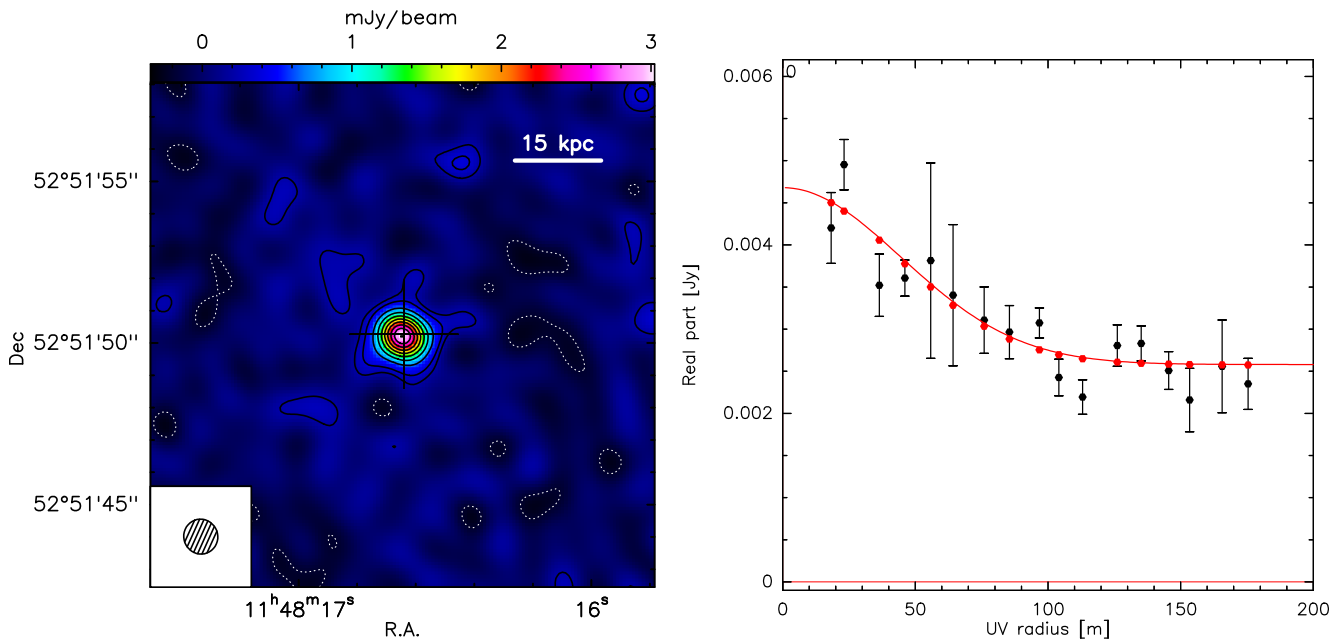


Fig. 11: IRAM PdBI map (*left*) and uv plane analysis (*right*) of the FIR continuum of SDSS J1148+5152 at average rest-frame wavelength $\lambda = 155 \mu\text{m}$. *Left*: Negative and positive contours correspond to -3σ , 3σ , 5σ to 45σ in steps of 5σ (1σ rms noise is $0.067 \text{ mJy beam}^{-1}$). The synthesized beam is shown at the bottom left corner ($1.1'' \times 1.1''$). *Right*: Real part of visibilities as a function of the uv distance (uv plot), binned in baseline steps of 10m. The red curve indicates the best fit to the uv plot, which corresponds to the sum of two components: a point (unresolved) source, responsible for the flattening of the visibilities at large uv radii (uv radii $> 100 \text{ m}$), and an extended (resolved) source fitted with a circular Gaussian model, which is responsible for the decreasing trend at smaller uv radii.

some irregular velocity pattern is observed, possibly associated with some minor mergers. This implies that it is difficult to estimate the dynamical mass of this system on large scales.

3.5. Analysis of the FIR continuum extent

We investigate the presence of extended dust emission in SDSS J1148+5152 by using ancillary high sensitivity IRAM PdBI observations of the FIR continuum in this source obtained as a part of a parallel project presented by Gallerani et al., (in prep) (see also Section 2). The deep observations by Gallerani et al. are particularly suited for studying the extent of the FIR continuum in SDSS J1148+5152, as they reach a continuum sensitivity of $0.067 \text{ mJy beam}^{-1}$ and have a slightly higher spatial resolution (synthesised beam of $1.1'' \times 1.1''$) than our main dataset.

The left panel of Figure 11 shows the map of the FIR continuum emission of SDSS J1148+5152 at a rest-frame wavelength of $\lambda = 155 \mu\text{m}$. This was produced by merging two datasets obtained with the IRAM PdBI at 262 GHz and 259.4 GHz. The corresponding uv visibility diagram is shown in the right panel of Fig. 11. Similarly to the narrow [C II] $158 \mu\text{m}$ emission (Figure 9), also the dust thermal emission can be disentangled in the uv data into a compact (unresolved) and an extended (resolved) component. Accordingly, we fit the uv plot of the $155 \mu\text{m}$ FIR continuum with a combination of a point source model and a circular Gaussian model, and show the best fit as a red curve in Fig 11. We stress that, although the circular Gaussian model provides a good fit to the data, it constitutes a simplistic approximation, and better quality data may reveal a more complex structure. The uv fit indicates that about 45% of the FIR emission at this wavelength is in the extended source, and it provides a FWHM size for the circular Gaussian component of (2.0 ± 0.4)

arcsec, corresponding to $(11 \pm 2) \text{ kpc}$. Taken at face value, this result suggests that the narrow [C II] ($\text{FWHM} = 17.4 \pm 1.7 \text{ kpc}$) extends beyond the region of intensive and high surface density star formation in the host galaxy of SDSS J1148+5152, traced by the FIR continuum emission ($\text{FWHM} = 11 \pm 2 \text{ kpc}$) (see also discussion in Section 4).

We use the uv fit results to produce separate maps of the extended and compact FIR sources, which are presented in Fig. 12. Strikingly, the resolved component exhibits a tail extending by $r \sim 12 \text{ kpc}$ in the western direction, i.e. the same direction as the $r \sim 28 \text{ kpc}$ filament observed in the map of the extended [C II] (Figure 10). This suggests that the western [C II] filament embeds star formation heating dust on $r \gtrsim 10 \text{ kpc}$ scales.

In order to estimate the FIR luminosity associated with the extended and compact dust continuum sources, we apportion the total FIR luminosity of SDSS J1148+5152, $L_{\text{FIR}(42.5-122.5\mu\text{m})} = (1.339 \pm 0.003) \times 10^{13} L_{\odot}$ (Valiante et al. 2011), according to the flux ratio estimated from our uv modelling of the FIR emission at $155 \mu\text{m}$ (Figure 11). This results into FIR ($42.5 - 122.5 \mu\text{m}$) luminosities of $L_{\text{FIR,ext}} = (6.0 \pm 0.8) \times 10^{12} L_{\odot}$ and $L_{\text{FIR,point}} = (7.4 \pm 0.8) \times 10^{12} L_{\odot}$ for the extended and compact component, respectively.

4. Discussion

4.1. The driving mechanism of the outflow

The models that have been proposed so far to explain AGN-driven kpc-scale outflows can be branched into two main categories: the so-called “blast - wave” models, in which large scale outflows are generated by hydrodynamical coupling of the AGN with the galaxy ISM through fast winds originating from the ac-

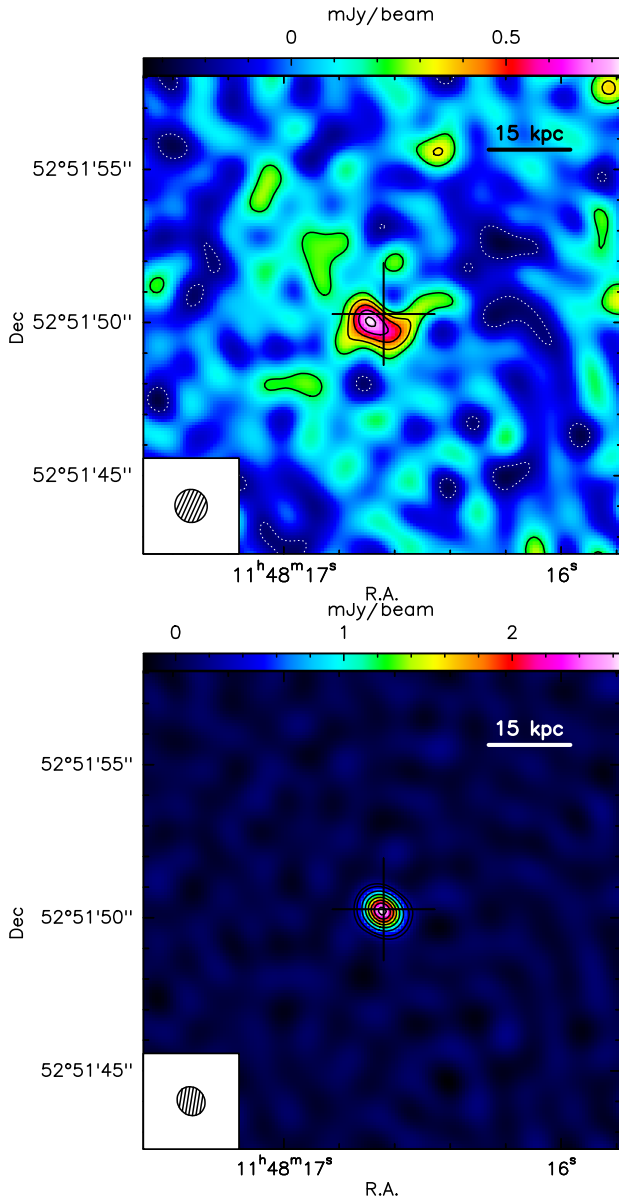


Fig. 12: Maps of the extended (*top*) and compact (*bottom*) components that contribute to the FIR continuum emission of SDSS J1148+5152 at average rest-frame wavelength $\lambda = 155 \mu\text{m}$. The map of the extended component has been obtained by subtracting, from the uv data, the point source model of the compact component resulting from the uv fit reported in Fig. 11. The map of the compact component has been obtained by applying a uv tapering that cuts visibilities with uv radius $< 100 \text{ m}$, therefore slightly increasing the resolution of the data (the resulting beam size is $1.0'' \times 0.9''$). In the map of the extended component, contours correspond to -3σ , 3σ , 5σ to 11σ in steps of 2σ (1σ rms noise is $0.067 \text{ mJy beam}^{-1}$). For the compact component, contours correspond to -3σ , 3σ , 5σ to 35σ in steps of 5σ (1σ rms noise is $0.072 \text{ mJy beam}^{-1}$).

cretion disk (e.g. King 2003, 2005, 2010; Lapi et al. 2005; Menci et al. 2006, 2008; Zubovas & King 2012, 2014; Faucher-Giguère & Quataert 2012; Costa et al. 2014 and references therein), and the models invoking radiation pressure on dusty clouds as the main mechanism at the origin of galactic-scale outflows (e.g. Hopkins & Elvis 2010; Fabian 2012; Roth et al. 2012; Thompson et al. 2014 and refs therein). In the recent years, both classes

of models have been tested against observations of AGN-driven outflows and, in particular, of massive kpc-scale outflows of cold and dense molecular gas in nearby galaxies (Feruglio et al. 2010, 2013a,b; Alatalo et al. 2011; Sturm et al. 2011; Aalto et al. 2012; Veilleux et al. 2013; Spoon et al. 2013; Combes et al. 2013; Ciccone et al. 2012, 2014; Garcia-Burillo et al. 2014). A recent study by Ciccone et al. (2014) showed that the “blast-wave” scenario and, specifically, the “energy-conserving” nature of the observed large-scale molecular outflows is favoured when considering a consistent sample of (U)LIRGs and powerful QSOs in the local Universe. However, there are only a few studies investigating the feedback mechanisms in high- z sources and, in particular, the detail of information provided by our new [C II] observations of SDSS J1148+5152 is unprecedented. In this section we discuss our results, presented in Section 3.3, in the light of the proposed theoretical models for AGN-driven outflows.

In this context, theoretical works have shown that there are three main properties of outflows, namely the mass-loss rate, the momentum rate (or momentum flux) and the kinetic power, that can be used as “key” indicators for the dominant feedback mechanism in action. In Section 3.3 and Appendix B we have used our new [C II] observations to infer these properties (both integrated and as a function of dynamical time-scale and radius) for the very extended outflow in SDSS J1148+5152. Bearing in mind that these are lower limits (because of the caveats discussed in Section 3.3 and Appendix B), the *integrated* values that we have obtained, do not help much in discriminating between different models. In particular, the modest integrated momentum rate of $(1.00 \pm 0.14) L_{\text{AGN}}/c$ and kinetic power of $(1.6 \pm 0.2) \times 10^{-3} L_{\text{AGN}}$ would be in principle consistent with any of the proposed models. However, the unprecedented spatial extent of the outflow in SDSS J1148+5152 has allowed us, for the first time, to go beyond the integrated values by investigating the dependence of the outflow properties as a function of the dynamical time-scale of the outflow and of the distance from the QSO (Figures 7 and 8).

The plots in Fig. 8, in particular, allow a direct comparison with the predictions of two recent studies, Costa et al. (2014), who incorporate the sub grid physics representing the “blast wave” feedback prescriptions into cosmological simulations, and Thompson et al. (2014), who further develop the physics of dusty radiation-pressure driven shells and discuss it in the context of the most recent observational results. Our results appear qualitatively inconsistent with the results obtained by Costa et al. (2014) from cosmological simulations of energy-driven outflows generated by inner accretion disk winds, which instead show that, on the same physical scales of $\lesssim 30$ (proper) kpc, the momentum flux and kinetic power of the outflow overall increase with radial distance from the AGN (Figure 15 of Costa et al. (2014)). Moreover, quantitatively, the outflow momentum rate and kinetic power inferred for SDSS J1148+5152 are about one order of magnitude lower than the integrated values reported by Costa et al. (2014) for the same simulation. We note however that the previously mentioned results by Costa et al. (2014) were obtained using a central black hole with mass of $\sim 10^8 M_{\odot}$, i.e. significantly lower than the BH mass of $\sim 3 \times 10^9 M_{\odot}$ estimated for SDSS J1148+5152 (Willott et al. 2003). Simulations may produce significantly different results for more massive halos and BHs. For example, Costa et al. (2014) show that, in presence of a more massive BH ($M_{\text{BH}} \sim 10^9 M_{\odot}$), even in the “momentum-driven” limit, i.e. the limit in which the thermal energy input from the inner wind is not conserved, efficient large scale AGN-driven outflows may develop, comparable to those developed under “energy-conserving” conditions. In this

case, by definition, the momentum flux would be of the order of L_{AGN}/c , consistently to what we infer for SDSS J1148+5152.

Costa et al. (2014) also show that, when an AGN-driven outflow develops, regardless of its momentum- or energy-conserving nature, its morphology is highly anisotropic and it strongly depends on the cosmological environment. In particular, the outflow develops preferably along “lower density” paths, free from filamentary cosmic inflows or from regions characterised by large amounts of dense gas in the halo or in the host galaxy. Interestingly, by comparing the maps in Fig. 4 and the top panel of Fig. 10, we note that the peak of the outflow component does not coincide with the peak of the narrow extended component. On the contrary, the narrow extended component (top panel of Fig. 10) peaks to the south-east with respect to the QSO position, where the outflow appears suppressed. If assuming that the emission within $v \in (-200, 200) \text{ km s}^{-1}$ is not significantly contaminated by the outflow, this result would support the scenario in which the outflow develops preferably in directions avoiding high density regions in the galaxy or in the halo.

We now consider the second class of models of AGN-driven outflows, i.e. models of outflows generated by coupling of the AGN radiation to dusty interstellar medium at galactic ($\sim \text{kpc}$) scales. More specifically, we refer to the work by Thompson et al. (2014), who have further developed the physics on which these models are based, demonstrating that dusty radiation-pressure driven shells can reach high velocities ($v_{\text{out}} \gg v_{\text{esc}}$). The predictions of Thompson et al. (2014) are qualitatively consistent with our observations of the outflow in SDSS J1148+5152, as shown by a comparison between our Fig. 8 and Fig. 3 of their paper. In particular, the decreasing trend with R and the modest (although lower limit) value of the momentum flux inferred for SDSS J1148+5152 could be explained by dusty radiation-pressure driven shells without resorting to extreme ISM conditions such as $\tau_{\text{IR}} \gg 1$. Our resolved FIR continuum observations (Figure 12) show that large amounts of dust are indeed present in this source. However, the FIR emission, indicating the presence of warm dust, extends only up to *maximum* radial distances of $r \approx 10 \text{ kpc}$ from the nucleus, while the outflow extends up to $r \approx 30 \text{ kpc}$.

4.2. The $[\text{C II}]$ -to-FIR luminosity ratio

In Section 3.4 and 3.5 we have shown a method, based on the uv visibility analysis, for decomposing both the narrow $[\text{C II}]$ emission and the FIR continuum emission of SDSS J1148+5152 into an extended (resolved) and a compact (unresolved) component. Following this decomposition, we estimate the $[\text{C II}]$ -to-FIR luminosity ratios separately for these two components. We obtain $\log(L_{[\text{C II}]} / L_{\text{FIR}})_{\text{EXT}} = -2.95^{+0.07}_{-0.08}$ and $\log(L_{[\text{C II}]} / L_{\text{FIR}})_{\text{POINT}} = -3.34^{+0.05}_{-0.05}$. These estimates are compared in Fig. 13 with $L_{[\text{C II}]} / L_{\text{FIR}}$ measurements obtained for local and distant galaxies.

We stress that the $L_{[\text{C II}]} / L_{\text{FIR}}$ values reported in Fig. 13 refer to the compact and extended components of the *narrow* $[\text{C II}]$ emission in SDSS J1148+5152, integrated within $(-200, 200) \text{ km s}^{-1}$. By selecting only the emission within this narrow velocity range, we intend to avoid contamination by the outflow, whose contribution to the $[\text{C II}]$ flux may be significant already at velocities $|v| > 200 \text{ km s}^{-1}$, as shown in Appendix B. However, the reader should be aware that, by selecting a wider velocity range for the $[\text{C II}]$ emission, the ratio $L_{[\text{C II}]} / L_{\text{FIR}}$ would naturally increase, especially for the extended component. In particular, by selecting the $[\text{C II}]$ emission within $(-300, 400) \text{ km s}^{-1}$, we

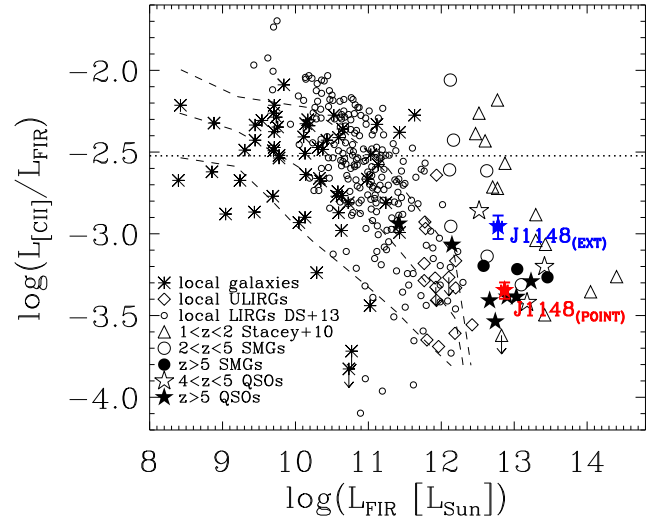


Fig. 13: $[\text{C II}]/\text{FIR}$ luminosity ratio as a function of FIR luminosity, with our new estimate of $L_{[\text{C II}]} / L_{\text{FIR}}$ in SDSS J1148+5152, obtained separately for the extended and compact components, as explained in Section 4.2. For comparison, the plot also includes previous ISO observations of local star-forming galaxies (asterisks, Malhotra et al. 2001) and of local ULIRGs (diamonds, Luhman et al. 2003) along with their median and scatter (dashed lines), recent Herschel-PACS observations of local LIRGs (small open circles, Díaz-Santos et al. 2013), the CSO-ZEUS survey of star forming and active galaxies at redshift $1 < z < 2$ (triangles, Stacey et al. 2010), observations of sub-millimeter galaxies (SMGs) at $2 < z < 5$ (open circles, Ivison et al. 2010; De Breuck et al. 2011; Valtchanov et al. 2011; Cox et al. 2011; Swinbank et al. 2012; Carniani et al. 2013), sub-millimeter galaxies (SMGs) at $z > 5$ (filled circles, Riechers et al. 2013, 2014, Neri et al. 2014), QSOs at $2 < z < 5$ (open stars, Maiolino et al. 2009; Wagg et al. 2010; Carniani et al. 2013), and $z > 5$ QSOs (filled stars, Venemans et al. 2012; Wang et al. 2013; Willott et al. 2013). The dotted horizontal line indicates the Milky Way value ($L_{[\text{C II}]} / L_{\text{FIR}} \sim 3 \times 10^{-3}$, Carilli & Walter 2013). All measurements refer to the FIR luminosity as integrated over $42.5\text{--}122.5 \mu\text{m}$. Where necessary, we have converted $L_{\text{FIR}(40\text{--}500\mu\text{m})}$ and $L_{\text{TIR}(8\text{--}1000\mu\text{m})}$ into $L_{\text{FIR}(42.5\text{--}122.5\mu\text{m})}$ by using the conversion factors provided by Carilli & Walter (2013), i.e. $L_{\text{FIR}(40\text{--}500\mu\text{m})} \approx 1.2 L_{\text{FIR}(42.5\text{--}122.5\mu\text{m})}$ and $L_{\text{TIR}(8\text{--}1000\mu\text{m})} \approx 1.3 L_{\text{FIR}(40\text{--}500\mu\text{m})}$.

obtain $\log(L_{[\text{C II}]} / L_{\text{FIR}})_{\text{EXT}} = -2.79^{+0.07}_{-0.08}$ and $\log(L_{[\text{C II}]} / L_{\text{FIR}})_{\text{POINT}} = -3.26^{+0.05}_{-0.05}$, corresponding to an increase of $L_{[\text{C II}]} / L_{\text{FIR}}$ by a factor of (1.4 ± 0.3) and by a factor of (1.20 ± 0.19) for the extended and compact components, respectively.

The $[\text{C II}]$ -to-FIR luminosity ratio is related to the contribution of the $[\text{C II}]$ line emission to the cooling of the (neutral) ISM in comparison to the cooling via dust grains as traced by the FIR emission. In local galaxies, early ISO observations and, more recently, Herschel observations, have established a clear trend for decreasing $[\text{C II}]$ -to-FIR ratio with increasing FIR luminosity (Luhman et al. 2003; Brauher et al. 2008; Díaz-Santos et al. 2013). The decreasing trend is even more evident for $L_{[\text{C II}]} / L_{\text{FIR}}$ as a function of $L_{\text{FIR}} / M_{\text{H}_2}$ (Graciá-Carpio et al. 2011). In particular, in local LIRGs and ULIRGs, $L_{[\text{C II}]} / L_{\text{FIR}}$ drops by about one order of magnitude with respect to normal disk galaxies, and this

deficiency is also extended to other FIR fine structure lines such as the [O I] 63 μm and [N II] 122 μm emission lines.

Lower [C II] -to-FIR ratios are most likely associated with intense star formation activity occurring in compact and warm starbursts (Díaz-Santos et al. 2013). More specifically, in compact starbursts, the main factors that can act to reduce the [C II] emission with respect to the FIR emission are: (i) high gas volume densities ($n \gg n_{\text{cr}}^{[\text{CII}]}$), for which the level populations of the C⁺ atoms ratio as their statistical weights, and thus the [C II] intensity becomes almost insensitive to higher gas volume densities and higher FUV fluxes (Wolfire et al. 1989); (ii) high ratios of FUV intensity field to the total hydrogen gas volume density, which would increase the positive charge of dust grains, thereby reducing the efficiency of gas heating via photo-electrons released by dust grains and so the relative efficiency of cooling via [C II] emission with respect to dust cooling (Luhman et al. 2003; Díaz-Santos et al. 2013); (iii) a high ionisation parameter U (which is essentially linked to (ii)) that reduces the opacity of hydrogen atoms (because a high fraction of H I is ionised) with respect to the dust opacity, hence increasing the fraction of UV photons absorbed by dust. Additionally, the incident UV radiation heats the dust to higher temperatures (Abel et al. 2009; Graciá-Carpio et al. 2011).

However, a relation between the [C II] luminosity and the FIR luminosity has not been clearly established for high redshift infrared luminous galaxies, which display a large scatter in the $L_{[\text{CII}]} / L_{\text{FIR}}$ vs L_{FIR} diagram (Graciá-Carpio et al. 2011), in some cases with values that are completely consistent with local disk galaxies, as also shown in Fig. 13. We find that, in the case of SDSS J1148+5152, the [C II] -to-FIR ratio in the compact source is lower than in the extended component, by a factor of ~ 3 (Figure 13). We note that a similar result has been obtained by Díaz-Santos et al. (2014) for the nuclear and extended components of local LIRGs observed with Herschel-PACS. This finding is consistent with a picture in which the nuclear [C II] and FIR emissions in SDSS J1148+5152 are excited by a compact “hyper-starburst” (Walter et al. 2009), similar to the nuclear regions of local ULIRGs, while the extended components trace more diffuse, “disk-like” star formation.

In Figure 14 we show the [C II] -to-FIR surface density ratio as a function of the projected distance from the QSO. The black curve is obtained by modelling in the uv data the [C II] and FIR extended components with circular Gaussian distributions (Sections 3.4 and 3.5), and it corresponds to:

$$\frac{\Sigma_{[\text{CII}]}(r)}{\Sigma_{\text{FIR}}}(r) = \frac{L_{[\text{CII}],\text{ext}}}{L_{\text{FIR},\text{ext}}} \left(\frac{\sigma_{\text{FIR}}^2}{\sigma_{[\text{CII}]}^2} \right) \exp \left[-r^2 \left(\frac{1}{2\sigma_{[\text{CII}]}^2} - \frac{1}{2\sigma_{\text{FIR}}^2} \right) \right], \quad (1)$$

where $L_{[\text{CII}],\text{ext}} = (6.7 \pm 0.7) \times 10^9 L_{\odot}$, $L_{\text{FIR},\text{ext}} = (6.0 \pm 0.8) \times 10^{12} L_{\odot}$, $\sigma_{[\text{CII}]} = (1.32 \pm 0.13)$ arcsec and $\sigma_{\text{FIR}} = (0.85 \pm 0.17)$ arcsec, as derived from the uv analysis. We remind that this model of $\Sigma_{[\text{CII}]} / \Sigma_{\text{FIR}}(r)$ is based on the narrow [C II] emission integrated within $(-200, 200)$ km s⁻¹, because in this velocity range the [C II] flux contamination by the outflow is low ($\lesssim 20\%$, according to the spectral decomposition shown in Fig. 1). Considering a larger velocity range for the [C II] emission would have as a main effect an upward shift of the relationship in Fig. 14. In particular, if taking into account the [C II] emission within $(-300, 400)$ km s⁻¹, $\Sigma_{[\text{CII}]} / \Sigma_{\text{FIR}}$ increases, at every radius, by a factor of ~ 1.4 .

The blue triangles in Fig. 14 show the $\Sigma_{[\text{CII}]} / \Sigma_{\text{FIR}}(r)$ ratio obtained by integrating the [C II] extended emission in the top panel of Fig. 10 over concentric annuli with $\Delta r = 0.4$ arcsec. These values follow quite well the black curve, at least up to

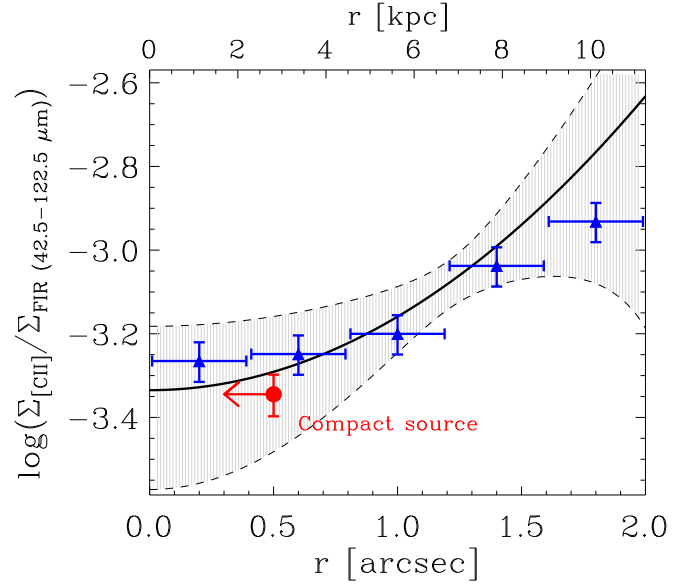


Fig. 14: [CII]/FIR luminosity surface density ratio as a function of the projected distance from the QSO optical position. The black curve represents our model of $\Sigma_{[\text{CII}]} / \Sigma_{\text{FIR}}(r)$ for the extended source, obtained from the analysis of the uv data as explained in Section 4.2. The grey shaded region indicates the statistical uncertainty on the $\Sigma_{[\text{CII}]} / \Sigma_{\text{FIR}}$ predicted by the model based on the uv analysis. The blue triangles show the values of $L_{[\text{CII}]} / L_{\text{FIR}}$ calculated at different radii by integrating the extended [CII] and FIR emission over concentric annuli. For comparison, the [CII]/FIR luminosity ratio of the compact (unresolved) component is also shown, plotted at a representative upper limit radius of $\text{FWHM}_{\text{beam}}/2$, where $\text{FWHM}_{\text{beam}}$ refers to the beam-size of the FIR continuum observations (Figure 11).

$r \approx 8$ kpc. We also show in Fig. 14 the $L_{[\text{CII}]} / L_{\text{FIR}}$ ratio obtained for the compact source, plotted in correspondence of an upper limit-radius of 0.5 arcsec (2.8 kpc), corresponding to half beam size. Interestingly, the [C II] -to-FIR ratio measured for the compact source is consistent with the value obtained for the extended source at a comparable r , strongly suggesting that the two components are powered by a similar mechanism (i.e. intense and compact star formation), at least up to ~ 5 kpc distance from the nucleus. At larger r , i.e. $5 < r[\text{kpc}] < 10$, $\Sigma_{[\text{CII}]} / \Sigma_{\text{FIR}}(r)$ increases to values more compatible with the disks of local galaxies (although still lower than the values measured in the Milky Way and in the bulk of local galaxies, see Figure 13), hinting at a less extreme star formation activity occurring on these scales. Understanding the origin of the [C II] emission at $r \gtrsim 10$ kpc is however more complex, and possible explanations are suggested in the Section 4.3.

4.3. Origin of the [C II] emission at $r \gtrsim 10$ kpc

Figure 14 shows that our model uncertainty for the [C II] -to-FIR surface density ratio increases significantly for $r \gtrsim 10$ kpc, and, in particular, no constraints can be put on $\Sigma_{[\text{CII}]} / \Sigma_{\text{FIR}}$ at such large radii. This is due to the fact that, above $r \sim 8 - 10$ kpc, the FIR continuum drops below our sensitivity and only [C II] is detected, as it can be clearly seen by comparing the upper panels of Figures 10 and 12. The abrupt drop of FIR surface density may indicate that, at $r \gtrsim 10$ kpc, the [C II] flux does not correlate with star formation (and so with the FIR emission) in the same way as

in the nuclear regions. In other words, extended [C II] emission at $r \gtrsim 10$ kpc may trace a different regime of star formation with respect to the central regions of the galaxy ($r < 5$ kpc) and also with respect to the regions at $5 < r[\text{kpc}] < 10$.

Furthermore, at $r \gtrsim 10$ kpc, a significant fraction of [C II] may trace a different ISM phase than dense PDRs. For example, [C II] may arise from diffuse HI (mostly cold neutral medium, CNM), diffuse molecular clouds and, in minor measure, diffuse warm ionised medium (WIM). This behaviour of [C II] has been observed in low metallicity systems such as Haro 11 and in the outskirts of the Milky Way and other local galaxies (Kramer et al. 2013; Parkin et al. 2013; Pineda et al. 2013; Langer et al. 2014). In particular, Kramer et al. (2013) have shown that the CNM contribution to [C II] in the outer regions of M33 increases by $\sim 25\%$ with respect to the inner region (i.e. $r < 2$ kpc). This effect is accompanied by an increase of $L_{[\text{CII}]} / L_{\text{FIR}}$ by almost a factor of 4 for $r > 4.5$ kpc, similarly to what we observe in SDSS J1148+5152, although in M33 the transition occurs at much smaller scales. Moreover, Pineda et al. (2013) and Langer et al. (2014) have shown that, in our Galaxy, a significant fraction of [C II] stems from CNM ($\sim 20\%$) and from “CO-dark” molecular gas ($\sim 30\%$), which dominates the gas mass of diffuse and “warm” molecular clouds (i.e. a transition phase between diffuse HI clouds and dense CO-bright molecular clouds), and these fractions increase with increasing galactocentric distance. In addition, Vallini et al. (2013) have shown through radiative transfer simulations of the ISM in Himiko (Ouchi et al. 2013) that [C II] emission may arise from the CNM residing at the periphery ($r \gtrsim 5$ kpc) of the galaxy.

However, we note that the [C II] surface density that we measure in the extended component of SDSS J1148+5152 is still three orders of magnitude higher than what observed in the outskirts of local galaxies. This implies that the contribution of different ISM phases to the [C II] emission discussed above is not sufficient to justify the extended [C II] flux - with no significant associated FIR emission - observed at $r \gtrsim 10$ kpc in SDSS J1148+5152. Therefore, although a comparison with the local Universe may help understanding what we observe in SDSS J1148+5152, we should keep in mind that the galactic environment of a luminous QSO at $z > 6$ can be very different even from the most extreme galaxies that we observe locally, and even more so from the Milky Way or other local disks such as M33 and M51.

In order to clarify the origin of the extended [C II] emission at $r > 10$ kpc, high sensitivity and multi-wavelengths observations are needed. In particular, while our IRAM PdBI observations prove, for the first time, that cold gas (both in outflow and not) extends up to $r \sim 30$ kpc in the host galaxy of SDSS J1148+5152, corresponding to about 1/3 of the virial radius estimated for its massive halo (Valiante et al. 2011, 2014), it is still not clear how [C II] can be excited up to such large distances from the central starburst. In summary, whether associated with dense PDRs or with a more diffuse ISM phase, the extended - and relatively high surface density - [C II] emission discovered in SDSS J1148+5152 requires an excitation source. This may be provided by in situ star formation, by the nuclear starburst, by the QSO and/or by strong shocks.

5. Summary and conclusions

We have presented follow-up C and D configuration IRAM PdBI observations of the [C II] $158\mu\text{m}$ fine structure line and FIR continuum in the host galaxy of the luminous quasar SDSS J1148+5152 at redshift $z=6.4189$. The total

[C II] velocity-integrated flux of 34 ± 9 Jy km s $^{-1}$, estimated by using a spectrum extracted from a circular aperture with a diameter of 8 arcsec, is significantly larger than any previous measurement of the same source. This clearly indicates the presence, in the QSO host galaxy, of additional baryonic mass (in cold gas) that was missed by previous observations with a lower sensitivity to large scale structures. The [C II] spectrum shows broad emission extending from -1400 km s $^{-1}$ to 1200 km s $^{-1}$ from the systemic velocity, confirming the detection of a powerful outflow by Maiolino et al. (2012). The total continuum-subtracted map shows a very extended [C II] source, with filamentary structures extending up to the extreme distance of $r \sim 30$ kpc from the position of the QSO.

We have further investigated the properties of the outflow, and we have found that:

- The outflow is resolved at high significance by our observations, revealing an extremely complex morphology, butterfly-like, with filaments extending up to $r \approx 30$ kpc from the nucleus.
- Although the median outflow dynamical time-scale is $\tau_{\text{dyn}}^{\text{median}} = 25$ Myr, the distribution of τ_{dyn} within the outflow is quite broad, ranging from ~ 4 Myr to ~ 100 Myr, indicating that the outflow has been in place for at least 100 Myr, which is a non-negligible fraction of the age of the Universe at this redshift.
- Our new estimates of the lower limits on the *integrated* mass-loss rate, momentum rate and kinetic power of the outflow are of $1400 \pm 300 M_{\odot} \text{ yr}^{-1}$, $(1.00 \pm 0.14) L_{\text{AGN}}/c$ and $(1.6 \pm 0.2) \times 10^{-3} L_{\text{AGN}}$, respectively.
- We have investigated, for the first time in an external galaxy, the outflow properties as a function of the dynamical time-scale and of the projected distance from the QSO. The results suggest that the ejection of gas in this source has not occurred at a constant rate, but most likely through multiple outflow events. In particular, we have found that the bulk of the mass, energy and momentum in this source have been released within the past ~ 20 Myr.

We have discussed the outflow properties in the light of theoretical models for AGN-driven outflows. We have noted that the *integrated* outflow momentum rate of $(1.00 \pm 0.14) L_{\text{AGN}}/c$ and kinetic power of $(1.6 \pm 0.2) \times 10^{-3} L_{\text{AGN}}$ are quite modest compared to local ULIRGs /QSOs and in principle consistent with any of the proposed models of AGN-driven outflows. By considering the mass-loss outflow rate, momentum rate and kinetic power of the outflow as a function of the distance from the QSO, we have found that observations are qualitatively consistent with radiation-pressure driven dusty shells. However, we have also found that the morphology and distribution of the outflow is consistent with recent cosmological simulations involving energy-driven outflows. Yet, a more quantitative comparison with the latter studies requires simulations matching the properties of this specific object (halo mass, SMBH mass).

Quite surprisingly, we have discovered that not only the outflow, but also the quiescent gas at systemic velocity is extremely extended in this source. More specifically, we have found that the [C II] emission within $v \in (-200, 200)$ km s $^{-1}$ traces two components:

- (i) A compact source, not resolved at our spatial resolution of ~ 1.2 arcsec, which corresponds to the 1.5 kpc size nuclear “hyper-starburs” detected by previous observations;
- (ii) An extended source with a FWHM size of 3.1 ± 0.3 arcsec, corresponding to 17.4 ± 1.7 kpc. The map of this component

reveals a complex structure, with a prominent filament extending up to $r \simeq 28$ kpc to the west (with respect to the QSO position). Strikingly, this extended component contributes to almost $\sim 70\%$ of the $[\text{C II}]$ flux within $v \in (-200, 200) \text{ km s}^{-1}$.

By using ancillary deep FIR continuum observations at $\lambda_{\text{rest}} = 155 \mu\text{m}$, we have found that also the FIR emission from dust can be disentangled into a compact and a more extended component contributing to 45% of the total FIR emission at this wavelength. The extended FIR component has a FWHM size of (11 ± 2) kpc, with a tail extending by $r \sim 12$ kpc to the west, and it has therefore a smaller extent than the extended $[\text{C II}]$ source.

We have estimated the $[\text{C II}]$ -to-FIR surface density ratio as a function of the distance from the QSO, and we have found that, within $r \lesssim 5$ kpc, $\Sigma_{[\text{C II}]} / \Sigma_{\text{FIR}}$ is low ($\simeq 5 \times 10^{-4}$) and similar for the compact and extended sources, indicating that they are likely both powered by an intense and compact starburst. At intermediate radii, i.e. $5 < r [\text{kpc}] < 10$, $\Sigma_{[\text{C II}]} / \Sigma_{\text{FIR}}$ increases up to $\simeq 1.1 \times 10^{-3}$, suggesting the presence of less extreme star formation activity on these scales. At larger radii, i.e. $r \gtrsim 10$ kpc, the FIR continuum drops below our sensitivity and only $[\text{C II}]$ is detected. This indicates that at such large distances from the galaxy centre, the $[\text{C II}]$ emission does not correlate with FIR continuum and with star formation in the same way as in the central regions. Moreover, similarly to the outskirts of local galaxies and to low metallicity systems, a large fraction of $[\text{C II}]$ at $r \gtrsim 10$ kpc may arise from different phases of the ISM than dense PDRs, such as diffuse atomic or molecular gas clouds. However, how $[\text{C II}]$ emission can be excited up to such large distances from the QSO and from the intense central starburst remains obscure, and additional observations with the future facilities such as NOEMA are needed to answer this question.

Acknowledgements. This work is based on observations carried out with the IRAM Plateau de Bure Interferometer. IRAM is supported by INSU/CNRS (France), MPG (Germany) and IGN (Spain).

References

- Aalto, S., García-Burillo, S., Müller, S., et al. 2012, *A&A*, 537, A44
 Abel, N. P., Dudley, C., Fischer, J., Satyapal, S., & van Hoof, P. A. M. 2009, *ApJ*, 701, 1147
 Alatalo, K., Blitz, L., Young, L. M., et al. 2011, *ApJ*, 735, 88
 Appleton, P. N., Guillard, P., & Boulanger, F. e. a. 2013, *ApJ*, 777, 66
 Bertoldi, F., Carilli, C. L., Cox, P., et al. 2003, *A&A*, 406, L55
 Brauer, J. R., Dale, D. A., & Helou, G. 2008, *ApJS*, 178, 280
 Calura, F., Gilli, R., Vignali, C., et al. 2014, *MNRAS*, 438, 2765
 Carilli, C. L. & Walter, F. 2013, *ARA&A*, 51, 105
 Carniani, S., Marconi, A., Biggs, A., et al. 2013, *A&A*, 559, A29
 Castro-Carrizo, A. & Neri, R. 2010, IRAM Plateau de Bure Interferometer Data Reduction Cookbook
 Cicone, C., Feruglio, C., Maiolino, R., et al. 2012, *A&A*, 543, A99
 Cicone, C., Maiolino, R., Sturm, E., et al. 2014, *A&A*, 562, A21
 Combes, F., García-Burillo, S., & Casasola, V. e. a. 2013, *A&A*, 558, A124
 Contursi, A., Poglitsch, A., Gracia Carpio, J., & Veilleux, S. e. a. 2013, *A&A*, 549, A118
 Costa, T., Sijacki, D., & Haehnelt, M. G. 2014, *ArXiv e-prints*
 Cox, P., Krips, M., Neri, R., et al. 2011, *ApJ*, 740, 63
 De Breuck, C., Maiolino, R., Caselli, P., et al. 2011, *A&A*, 530, L8
 De Breuck, C., Williams, R. J., Swinbank, M., et al. 2014, *A&A*, 565, A59
 Decarli, R., Walter, F., Yang, Y., et al. 2012, *ApJ*, 756, 150
 Díaz-Santos, T., Armus, L., Charmandaris, V., et al. 2013, *ApJ*, 774, 68
 Díaz-Santos, T., Armus, L., & Charmandaris, V. e. a. 2014, *ApJL*, 788, L17
 Fabian, A. C. 2012, *ARA&A*, 50, 455
 Fan, X., Strauss, M. A., & Schneider, D. P. e. a. 2003, *AJ*, 125, 1649
 Faucher-Giguère, C.-A. & Quataert, E. 2012, *MNRAS*, 425, 605
 Feruglio, C., Fiore, F., Maiolino, R., et al. 2013a, *A&A*, 549, A51
 Feruglio, C., Fiore, F., & Piconcelli, E. e. a. 2013b, *A&A*, 558, A87
 Feruglio, C., Maiolino, R., Piconcelli, E., et al. 2010, *A&A*, 518, L155+
 Fischer, J., Sturm, E., González-Alfonso, E., et al. 2010, *A&A*, 518, L41+
 Gallerani, S., Maiolino, R., Juárez, Y., & Nagao, T. e. a. 2010, *A&A*, 523, A85

- Gallerani, S., Neri, R., & Maiolino, R. e. a. 2012, *A&A*, 543, A114
 García-Burillo, S., Combes, F., & Usero, A. e. a. 2014, *ArXiv e-prints*
 Graciá-Carpio, J., Sturm, E., Hailey-Dunsheath, S., & Fischer, J. e. a. 2011, *ApJL*, 728, L7
 Hailey-Dunsheath, S., Nikola, T., Stacey, G. J., et al. 2010, *ApJL*, 714, L162
 Hopkins, P. F. & Elvis, M. 2010, *Monthly Notices of the Royal Astronomical Society*, 401, 7
 Ivison, R. J., Swinbank, A. M., Swinbank, B., et al. 2010, *A&A*, 518, L35
 King, A. 2003, *The Astrophysical Journal*, 596, L27
 King, A. 2005, *The Astrophysical Journal*, 635, L121
 King, A. R. 2010, *MNRAS*, 402, 1516
 Kramer, C., Abreu-Vicente, J., García-Burillo, S., & Relaño, M. e. a. 2013, *A&A*, 553, A114
 Kreckel, K., Armus, L., Groves, B., Lyubenova, M., & Díaz-Santos, T. e. a. 2014, *ApJ*, 790, 26
 Langer, W. D., Velusamy, T., Pineda, J. L., et al. 2010, *A&A*, 521, L17
 Langer, W. D., Velusamy, T., Pineda, J. L., Willacy, K., & Goldsmith, P. F. 2014, *A&A*, 561, A122
 Lapi, A., Cavaliere, A., & Menci, N. 2005, *ApJ*, 619, 60
 Luhman, M. L., Satyapal, S., Fischer, J., et al. 2003, *ApJ*, 594, 758
 Maiolino, R., Caselli, P., Nagao, T., et al. 2009, *A&A*, 500, L1
 Maiolino, R., Cox, P., Caselli, P., et al. 2005, *A&A*, 440, L51
 Maiolino, R., Gallerani, S., Neri, R., et al. 2012, *MNRAS*, 425, L66
 Malhotra, S., Kaufman, M. J., Hollenbach, D., et al. 2001, *ApJ*, 561, 766
 Menci, N., Fiore, F., Puccetti, S., & Cavaliere, A. 2008, *ApJ*, 686, 219
 Menci, N., Fontana, A., Giallongo, E., Grazian, A., & Salimbeni, S. 2006, *The Astrophysical Journal*, 647, 753
 Neri, R., Downes, D., Cox, P., & Walter, F. 2014, *A&A*, 562, A35
 Ouchi, M., Ellis, R., Ono, Y., & Nakanishi, K. e. a. 2013, *ApJ*, 778, 102
 Parkin, T. J., Wilson, C. D., Schirm, M. R. P., & Baes, M. e. a. 2013, *ApJ*, 776, 65
 Pineda, J. L., Langer, W. D., Velusamy, T., & Goldsmith, P. F. 2013, *A&A*, 554, A103
 Planck Collaboration, Ade, P. A. R., Aghanim, N., et al. 2013, *ArXiv e-prints*
 Riechers, D. A., Bradford, C. M., Clements, D. L., et al. 2013, *Nature*, 496, 329
 Riechers, D. A., Carilli, C. L., Capak, P. L., et al. 2014, *ArXiv e-prints*
 Riechers, D. A., Walter, F., Bertoldi, F., & Carilli, C. L. e. a. 2009, *ApJ*, 703, 1338
 Roth, N., Kasen, D., Hopkins, P. F., & Quataert, E. 2012, *ApJ*, 759, 36
 Schneider, R., Bianchi, S., Valiante, R., Risaliti, G., & Salvadori, S. 2014, *ArXiv e-prints*
 Spoon, H. W. W., Farrah, D., & Leboutteiller, V. e. a. 2013, *ApJ*, 775, 127
 Stacey, G. J., Hailey-Dunsheath, S., Ferkinhoff, C., et al. 2010, *ApJ*, 724, 957
 Sturm, E., González-Alfonso, E., & Veilleux, S. e. a. 2011, *ApJ*, 733, L16+
 Swinbank, A. M., Karim, A., Smail, I., et al. 2012, *MNRAS*, 427, 1066
 Thompson, T. A., Fabian, A. C., Quataert, E., & Murray, N. 2014, *ArXiv e-prints*
 Valiante, R., Schneider, R., Salvadori, S., & Bianchi, S. 2011, *MNRAS*, 416, 1916
 Valiante, R., Schneider, R., Salvadori, S., & Gallerani, S. 2014, *ArXiv e-prints*
 Vallini, L., Gallerani, S., Ferrara, A., & Baek, S. 2013, *MNRAS*, 433, 1567
 Valtchanov, I., Virdee, J., Ivison, R. J., et al. 2011, *MNRAS*, 415, 3473
 Veilleux, S., Melendez, M., Sturm, E., & Graciá-Carpio, J. e. a. 2013, *ArXiv e-prints*
 Velusamy, T., Langer, W. D., & Pineda, J. L. e. a. 2010, *A&A*, 521, L18
 Venemans, B. P., McMahon, R. G., Walter, F., et al. 2012, *ApJL*, 751, L25
 Wagg, J., Carilli, C. L., Wilner, D. J., et al. 2010, *A&A*, 519, L1
 Walter, F., Bertoldi, F., & Carilli, C. e. a. 2003, *Nature*, 424, 406
 Walter, F., Carilli, C., Bertoldi, F., et al. 2004, *ApJL*, 615, L17
 Walter, F., Riechers, D., Cox, P., et al. 2009, *Nature*, 457, 699
 Wang, R., Wagg, J., Carilli, C. L., et al. 2013, *ApJ*, 773, 44
 Willott, C. J., McLure, R. J., & Jarvis, M. J. 2003, *ApJL*, 587, L15
 Willott, C. J., Omont, A., & Bergeron, J. 2013, *ApJ*, 770, 13
 Wolfire, M. G., Hollenbach, D., & McKee, C. F. 2010, *ApJ*, 716, 1191
 Wolfire, M. G., Hollenbach, D., & Tielens, A. G. G. M. 1989, *ApJ*, 344, 770
 Zubovas, K. & King, A. 2012, *ApJL*, 745, L34
 Zubovas, K. & King, A. R. 2014, *MNRAS*, 439, 400

Appendix A: Spectral features in the extended $[\text{C II}]$ source

In Table A.1 we report the results of the spectral fitting to the bright features A-F of the extended $[\text{C II}]$ $158 \mu\text{m}$ source, shown in Fig. 3. It is immediately evident from Table A.1 that the features A-F are characterised, on average, by high velocity dispersions, which can be as high as $\sigma_v \sim 800 \text{ km s}^{-1}$, suggesting that they are mostly associated with the quasar-driven outflow discovered by Maiolino et al. (2012). This is confirmed by the analysis of the maps of the broad wings (Section 3.3). However, we note that, in correspondence of some positions (e.g. B, C, F), there is also a significant contribution from “narrow” emission at the systemic velocity, hinting at the presence of a very extended “quiescent” (i.e. non outflowing) $[\text{C II}]$ component, which is investigated in Section 3.4.

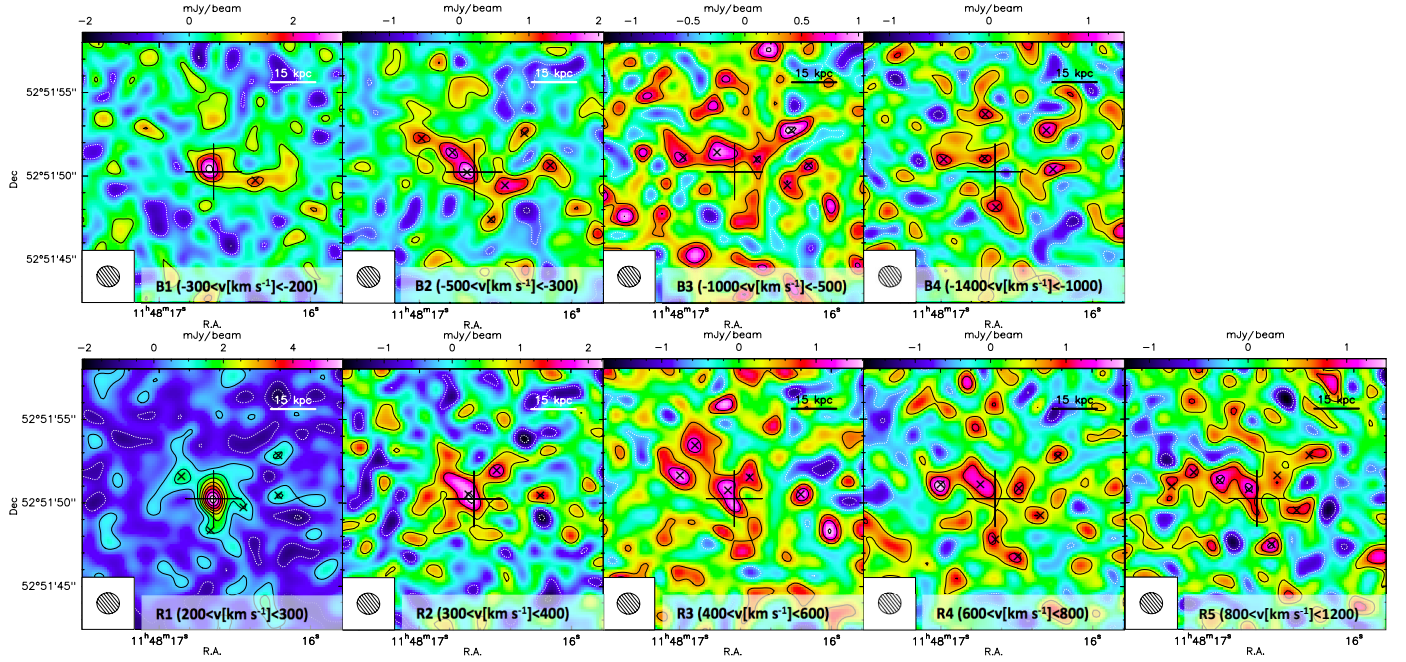


Fig. B.1: IRAM PdBI continuum-subtracted maps of the blue- (*top panels*) and red- (*bottom panels*) shifted [C II] 158 μ m emission of SDSS J1148+5152, obtained at different velocities. The corresponding velocity integration ranges are indicated on each map. Negative and positive contours are in steps of 1.5σ . The small crosses mark the position of the 48 blobs that we identified as belonging to the outflow. For each of these clumps in outflow we estimate the dynamical time-scale $\tau_{\text{dyn}} = R/v$, where R is the distance from the QSO position, and v is the average velocity of each map.

Table A.1: Results of the Gaussian fits to the spectra extracted from different positions on the source shown in Fig. 3

Pos [†]	v [km s ⁻¹]	σ_v [km s ⁻¹]	S_{peak} [mJy]	I_v [Jy km s ⁻¹]
A	-700 \pm 300	800 \pm 300	0.8 \pm 0.2	1.7 \pm 0.8
	1100 \pm 140	230 \pm 150	0.8 \pm 0.4	0.5 \pm 0.4
B	-170 \pm 40	110 \pm 50	2.7 \pm 1.0	0.7 \pm 0.4
	-300 \pm 400	800 \pm 400	0.9 \pm 0.5	1.7 \pm 1.3
C	-1120 \pm 110	210 \pm 120	1.5 \pm 0.7	0.8 \pm 0.6
	700 \pm 500	700 \pm 400	1.0 \pm 0.5	1.6 \pm 1.2
	130 \pm 100	140 \pm 120	1.4 \pm 1.0	0.5 \pm 0.6
D	-900 \pm 400	600 \pm 400	1.1 \pm 0.5	1.5 \pm 1.3
	800 \pm 200	500 \pm 200	1.6 \pm 0.5	1.9 \pm 1.1
	100 \pm 200	500 \pm 200	1.5 \pm 0.3	2.0 \pm 0.9
E	-1430 \pm 90	130 \pm 90	1.1 \pm 0.6	0.4 \pm 0.3
	100 \pm 200	500 \pm 200	1.5 \pm 0.3	2.0 \pm 0.9
	1200 \pm 200	300 \pm 200	0.7 \pm 0.6	0.5 \pm 0.5
F	110 \pm 80	220 \pm 80	1.9 \pm 0.5	1.0 \pm 0.5
	1100 \pm 90	100 \pm 90	1.0 \pm 0.7	0.3 \pm 0.3
	-800 \pm 500	400 \pm 600	0.4 \pm 0.4	0.3 \pm 0.7

Notes: [†] Each row corresponds to a Gaussian component. We note that in all cases the spectral fit requires multiple Gaussian components.

Appendix B: Outflow channel maps

In this section we explain the method we employ to estimate the outflow mass-loss rate using the resolved information provided by our IRAM PdBI observations. We produce channel maps of the [C II] 158 μ m blue- and red-shifted emission at velocities $v \leq -200$ km s⁻¹ and $v \geq 200$ km s⁻¹, respectively. The maps are shown in Fig. B.1. The channel widths vary with velocities, because we aim to obtain an approximately constant signal-to-

noise for the extended emission in each map. For this reason, at lower velocities, i.e. closer to the [C II] emission peak, we use narrow channels with $\Delta v = 100$ km s⁻¹, while at higher velocities, tracing the fainter high-velocity component of the outflow, we integrate over wider channels of $\Delta v \sim 200$ -500 km s⁻¹. The centroid positions of the 48 clumps that we ascribe to the outflow are indicated within the region corresponding to the total [C II] source shown in Fig. 2 and to have in the maps a signal-to-noise ratio $\text{SNR} \geq 3$. We note that we have conservatively excluded from the outflow computation the central components of maps B1 ($\langle v \rangle = -250$ km s⁻¹) and R1 ($\langle v \rangle = 250$ km s⁻¹), because, due to low velocities probed by these two maps, it is difficult to assess to which extent the central extended emission belongs to the outflow. For similar reasons we have not taken into account the central core emission within ± 200 km s⁻¹, although there may be a significant outflow contribution of $\sim 20\%$ even at these low velocities, as suggested by the Gaussian fits to the line profile (Figure 1). However, we have included in the outflow the central blobs visible in maps B2 and R2 (mean velocities of ± 350 km s⁻¹), because they are offset with respect to the QSO position and appear to be co-spatial with the higher velocity emission in maps B3 and R3, which is undoubtedly tracing the outflow.

For each blob (belonging to the outflow) we calculate from the maps its projected distance from the central QSO and, accordingly, obtain a measure of its dynamical time-scale. The dynamical time-scale is defined as $\tau_{\text{dyn}} = R/v$, where R is the distance travelled by the clump (assumed equal to the projected distance between the centroid of each clump and the optical position of the QSO) and v is the velocity of the gas. The error on R is estimated differently for resolved and unresolved clumps; in particular, for unresolved clumps, σ_R is the FWHM of the synthesised beam divided by the signal-to-noise ratio. For resolved

clumps, instead, we set $\sigma_R = (r_{\text{max}}^2 - (\text{FWHM}_{\text{beam}}/2)^2)^{1/2}$, where r_{max} is the maximum (projected) radius of the blob. We conservatively adopt for v the average (projected) velocity of each map. We note that the uncertainty on v , defined as $\sigma_v = \Delta v/2$, is obviously higher in the higher velocity maps, where we have integrated the emission over larger velocity channels (Δv). The distribution of τ_{dyn} that we measure within the outflow is shown in Fig. 6.

To estimate the mass of (atomic) gas in outflow, we first measure the [C II] flux associated with each outflowing clump, by using apertures centred on the positions of the crosses (indicated in Fig. B.1). We then convert the [C II] fluxes (integrated over their corresponding velocity ranges Δv) into [C II] $158\mu\text{m}$ luminosities, and the [C II] luminosities into (lower limits on the) atomic gas mass, following Hailey-Dunsheath et al. (2010) as explained in Section 3.3. By adding up the mass-loss rate contribution, i.e. $\dot{M}_{\text{out}} = M_{\text{out}}/\tau_{\text{dyn}}$, from all the 48 clumps in outflow, we obtain a total integrated outflow rate of $1400 \pm 300 M_{\odot} \text{ yr}^{-1}$. The error is simply $(\sum_{i=1}^{48} \sigma_{i, \dot{M}_{\text{out}}}^2)^{1/2}$, where $\sigma_{\dot{M}_{\text{out}}}$ is the uncertainty on \dot{M}_{out} for a given clump in outflow, obtained by propagating errors on τ_{dyn} and on the velocity-integrated flux associated with the clump. We note, however, that the uncertainty on the conversion from [C II] luminosity to atomic gas mass is not taken into account in our error estimate.

Appendix C: Moments maps

We show in Fig. C.1 the first and second moment maps of the [C II] emission within $v \in (-200, 200) \text{ km s}^{-1}$, obtained by applying a flux threshold of 2.8 mJy. The moments maps suggest that the bulk of [C II] does not trace gas in a regularly rotating disk. Our IRAM PdBI observations are dominated by the extended [C II] component which, in this velocity range, contributes to $\sim 70\%$ of the total flux (Section 3.4). It is however possible that the compact source, unresolved by our observations, is rotationally-supported, as suggested by Walter et al. (2009). Moreover, the first moment map shows a north-south velocity gradient south of the QSO position, with velocities ranging from 20 km s^{-1} to 100 km s^{-1} , whose origin is not clear. In conclusion, no constraints can be put on the total dynamical mass of the system from our [C II] observations.

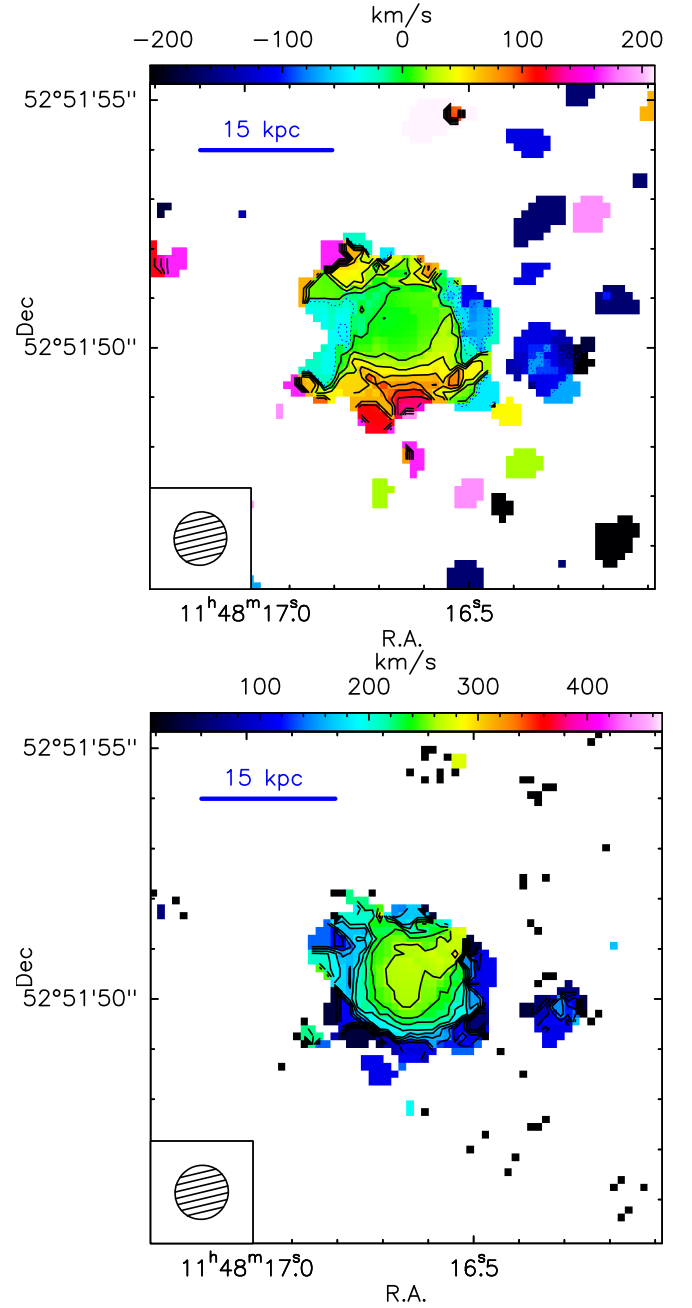


Fig. C.1: First (*top*) and second (*bottom*) moment maps obtained within $v \in (-200, 200) \text{ km s}^{-1}$ by applying a flux threshold of 2.8 mJy. Velocity contours in both maps are in steps of 20 km s^{-1} .